COUPLED AEROHEATING/ABLATION ANALYSIS FOR RE-ENTRY VEHICLES

Alvin Murray
ITT Aerotherm
6767 Old Madison Pike, Ste 310
Huntsville, AL 35806
256-964-1474
al.murray@itt.com

ABSTRACT

This paper demonstrates a new tool for analyzing an ablating material exposed to an aeroheating environment. This tool is the result of the coupling the thermal analysis capabilities of the Charring Material Ablation (CMA) finite difference code with the Maneuvering Aerotherm Shape Change Code (MASCC). MASCC represents the state-of-the-art in efficient aerothermal heating analysis. The code uses the axisymmetric analogy and solves the integral momentum and energy boundary layer equations along streamlines around the body. CMA was integrated into MASCC to provide a detailed 1D in-depth thermal solution with decomposing / charring materials. The surface temperature and ablation mass flux are explicitly coupled with the flowfield solution. The methodologies used in the new code are briefly summarized.

The capabilities of the Aeroheating and Thermal Analysis Code (ATAC) are demonstrated with two re-entry studies. The first study compares predictions with data taken for the Apollo program. Comparison will be made with wind tunnel pressure data, wind tunnel heat transfer data and with thermocouple data from actual Apollo flights. The second study was the design of the Entry, Descent, and Landing (EDL) vehicle for the Pascal Probe. Pascal was a proposed program to study the Martian atmosphere. ATAC was used to provide preliminary aerodynamic coefficients and heatshield sizing for the EDL. Comparisons were made with computational fluid dynamics and Free Molecular calculations throughout the reentry flight.

INTRODUCTION

The purpose of this paper is to describe a process for predicting the aeroheating and thermal response of blunt re-entry configurations in high-speed flows. These predictions are the required inputs to determine the survivability of a conceptual design and provide a needed evaluation of a design without having to build multiple prototypes for testing and evaluation. The flight regime of most interest is that of supersonic-hypersonic continuum flow in which the heat flux is sufficient to cause ablation at some locations on the surface.

In the past, flowfield solutions were generated during a specified flight using the Maneuvering Aerotherm Shape Change Code, MASCC.[1] At specified times, these boundary conditions were applied to a Charring Material Thermal Response and Ablation Program, CMA[2] finite difference model to obtain the transient thermal response at each of the surface nodes. The effects of changes in the surface temperature, ablation and pyrolysis mass fluxes, and the shape of the vehicle were not included in the analysis unless the user modified the MASCC input and re-ran the flowfield solutions. This would require a large number of CMA solutions to model the surface response and would be very labor intensive. The Aeroheating and Thermal Analysis Code (ATAC)[3] combines MASCC and CMA to provide an efficient and cost effective procedure for incorporating these effects into a thermal analysis. The methodologies used in ATAC are briefly described in the following sections.

FLOWFIELD ANALYSIS

ATAC includes a completely general three-dimensional flowfield solver that uses semiempirical procedures to determine the flowfield on missile configurations. The code offers significant efficiency advantages for design purposes over computational fluid dynamics (CFD) codes that solve the full Navier Stokes equations. The hundreds of flowfield and boundary layer solutions that are required to model a complete trajectory, requires only a few minutes with ATAC. CFD techniques, on the other hand, would require very fine grids to resolve boundary layers and this would result in extremely long run times to model the many different flight conditions that must be considered. Ideally, CFD techniques can be used in concert with ATAC to refine specific areas of complex flowfield phenomena and shock interactions when necessary.

ATAC can be used to calculate the surface heat flux based on the velocity, altitude, and angle of attack throughout the flight of interest. The basic inputs needed are the body configuration, angle of attack, and the freestream conditions. The geometry is described in ATAC with a system of Coon's bi-cubic patches[4]. These patches allow general geometries and facilitate the calculation of the surface coordinates and gradients at points intermediate to the nodal system. In ATAC, the axisymmetric analogy is used for the prediction of the flowfield. Using this approximation, the axisymmetric equations for the inviscid and viscous flow are integrated along various streamlines. An effective radius, or metric coefficient replaces the radius in the axisymmetric equations.

INVISCID STEAMLINE TRACING

The flowfield solution is performed along each of the calculated inviscid streamlines. The method used in ATAC to calculate these streamlines is known as the Newtonian approximation or the method of steepest descent. The Newtonian flow model assumes that a stream of particles impinging on a surface retains its tangential component of momentum. Therefore, an instantaneous velocity direction at each point on the body is defined by

$$\vec{v} = \hat{n} \times \left(\vec{V}_\infty \times \hat{n} \right)$$

By converting $\vec{v}$ to a unit tangent vector, the derivatives of the surface parameters with respect to the streamline arc length may be determined in the following manner. If $\vec{r}$ is the position vector of some point on the body, the parametric representation of the body geometry provides $\vec{r}$ as a function of the surface parameters *w* and *u*. The unit tangent vector at the point may then be written

$$\hat{t} = \frac{d\vec{r}}{ds} = \frac{\P \vec{r}}{\P w} \frac{dw}{ds} + \frac{\P \vec{r}}{\P u} \frac{du}{ds} \tag{1}$$

Any two of the three Equations (1) may be solved for dw/ds and du/ds, the slopes in each of the two surface coordinate directions. This algorithm can be started at any point on the body and integrated either upstream or downstream.

One of the most difficult problems in coupling a shape change procedure with a three-dimensional flowfield analysis is an accurate prediction of the environment at each shape change point. With a streamline tracing procedure, such as the one used in ATAC, this problem is even more complicated because the location of the streamlines is difficult to control as the nosetip ablates. The ATAC procedure begins at the back of the vehicle and traces a streamline forward to the stagnation point. This assures a reasonable distribution at the end of the vehicle and eliminates the effects of the ablated nosetip on the streamlines. To provide adequate coverage at the nosetip, a streamline addition procedure is used which establishes additional streamlines on the vehicle.

SURFACE PRESSURE

The ATAC code has three options for computing surface pressure distributions on the windward streamlines: (1) the Dahm-Love pressure correlations used in ASCC,[5] (2) a Newtonian pressure model with modifications for Mach number effects,[6] or (3) a modified Newtonian pressure model for sharp nosed vehicles.[7] Pressures on the leeward or shadow regions are calculated using: (1) the Newtonian approximation ($C_p = 0$), (2) hypersonic small disturbance theory,[8] or (3) a pressure correlation for separated flows.[8] In general, the Dahm-Love correlations are used for blunt, short, sphere-cone geometries. The modified Newtonian model is used for ogives and other sharp-nosed configurations.

SHOCK SHAPE

A thin-shock layer integral technique is used in ATAC to compute the shock shape. The global continuity and axial momentum equations are cast in integral form. The global continuity equation is given by:

$$r_\infty u_\infty p \; R^2 = 2p \int_0^{d_s} r u r dy$$

and the global axial momentum

$$\left(p_\infty + r_\infty u_\infty^2\right)pR^2 = \int_0^{d_s} ru\left(u\cos q + v\sin q\right)2prdy + \int_0^{s}\left(p_w \sin q\right)2pr_w ds + \int_0^{d_t}\left(p\cos q\right)2prdy$$

The integrands are assumed to vary linearly between the body surface and shock. The flow properties behind the shock are related to freestream conditions via oblique shock relations and the equation of state. With the known pressure distribution along the wall, together with the assumed integrand functional form and behind-the-shock properties, the continuity and axial momentum equations are solved for shock standoff distance and shock angle. The standoff distance and angle are related by geometry, which serves as a boundary condition, rendering an elliptic system of equations, which must be iterated for the standoff distance along the body. Decoupling the geometry constraint from the system of equations eliminates the iteration. This approach results in an initial value problem. The control volume for the thin shock layer solution is shown in Fig. 1.

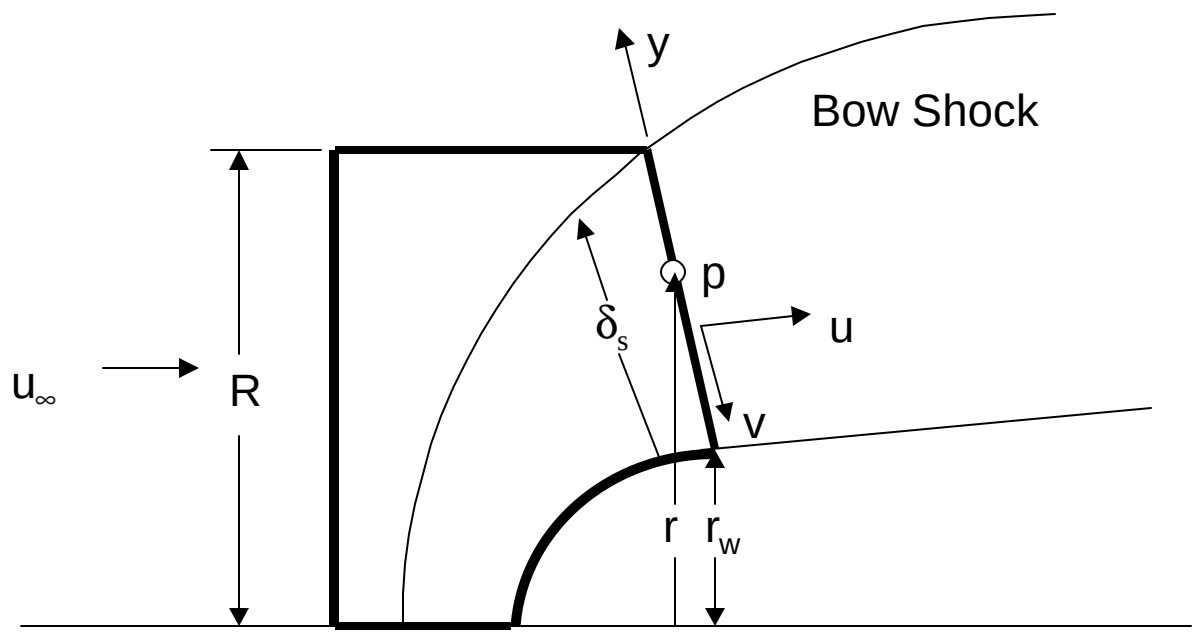

Figure 1: Control Volume for the Shock Shape Solution

BOUNDARY LAYER TECHNIQUE

The boundary layer scheme employed in ATAC is known as the Momentum /Energy Integral Technique (MEIT). MEIT has also been used in the ABRES Shape Change Code, ASCC[5] and Three Dimensional Momentum / Energy Integral Technique (3DMEIT) codes and is essentially the same in all of these procedures. The current modifications in ATAC incorporate the latest developments in MEIT and the procedure should be the same as that used in ASCC86 except for the metric coefficient and differences in the body slopes due to the different geometry specification. In MEIT, the baseline

relationships are those for C_f and C_h as functions of Re_q and Re_f on an incompressible flat plate.

The effects of other phenomena are included as multiplicative factors, called influence coefficients, which are applied to the baseline expressions. A theoretical justification for this approach is the work of Kutateladze and Leont'ev[9, 10] who show that the asymptotic behavior of the shear and heat transfer for compressible boundary layer flow over a flat plate in the limit of infinite Reynolds number differ from the corresponding incompressible case by a factor they call Ψ, which is exactly the influence coefficient used in MEIT.

The following three basic equations are solved simultaneously in the MEIT procedure:
Integral momentum equation:

$$\frac{1}{r r_e u_e^2}\frac{d}{ds}(r r_e u_e^2 \Theta) = \frac{C_f}{2} + \frac{(r\,v)_w u_{i,w}}{r_e u_e^2} + \frac{H\Theta}{r_e u_e^2}\frac{dp}{ds} \tag{2}$$

Integral energy equation:

$$\frac{1}{r r_e u_e (h_{t,e} - h_w)}\frac{d}{ds}\left(r r_e u_e \left(h_{t,e} - h_w\right)\Phi\right) = C_h \frac{h_r - h_w}{h_{t,e} - h_w} + \frac{(r\,v)_w \left(h_{t,i,w} - h_w\right)}{r_e u_e (h_{t,e} - h_w)} \tag{3}$$

Entrainment relation:

$$r_\infty u_\infty \bar{y}^2 = 2 r F m_e \,\mathrm{Re}_q - 2\int_0^\infty r\,(r\,v)_w\, ds \tag{4}$$

The momentum equation solution dictates the skin friction and momentum thickness upon which the following phenomena are based: 1) transition onset and location, 2) transitional intermittency, 3) surface roughness effects, 4) turbulent boundary layer shape factors, and 5) entrainment rate. The energy equation solution dictates the convective heat transfer subject to these five parameters.

The entrainment relation, Eq. (4), provides a means of determining the boundary layer edge properties that are essential boundary conditions for the solution of Eqs. (2) and (3). The boundary layer edge thermodynamic state is determined by lookup on pressure and entropy in a real-gas Mollier table. Pressure is known from the inviscid flow solution, and entropy is calculated from consideration of the bow shock shape and boundary layer mass entrainment. Figure 2 illustrates the method and basis for the mass balance that leads to Eq. (4).

BASIC BOUNDARY LAYER LAWS

The friction factor and Stanton number are represented by $C_{x,y,0}$ where the subscript 0 denotes the basic laws, x = f for friction factor and x = h for Stanton number. The state of the boundary layer is shown by the subscript y. Subscript ℓ is used for laminar flow and t for turbulent flow.

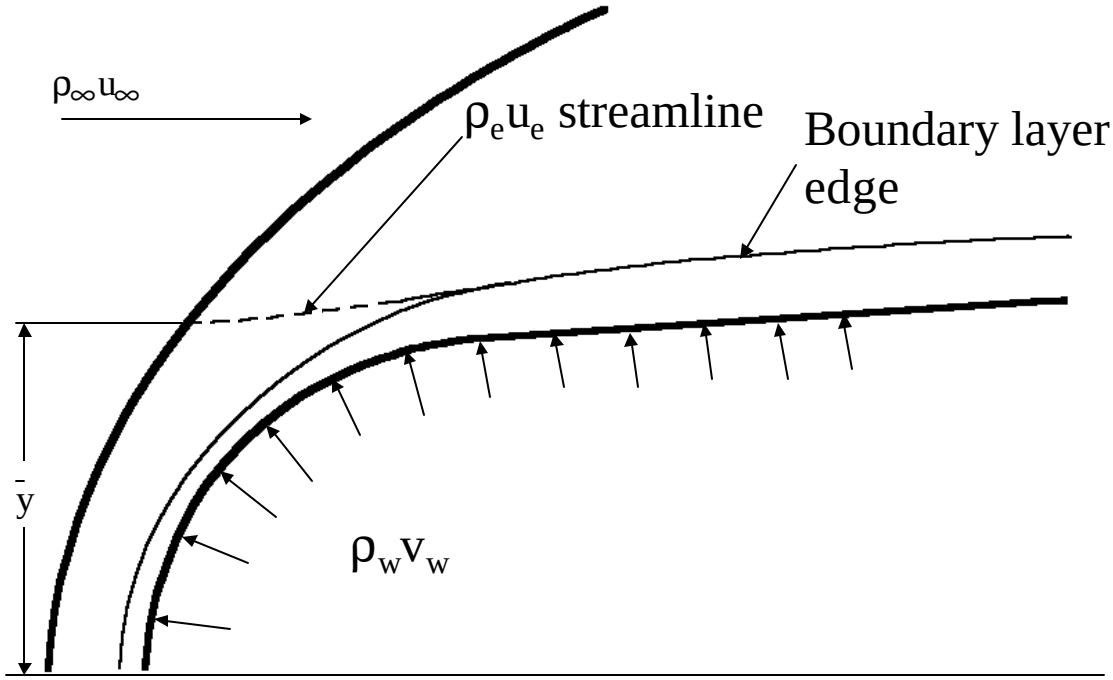

Figure 2: Sketch of the Boundary Layer Mass Entrainment Method

<u>Wall Shear and Heat Flux</u>

The basic laws for the friction and Stanton number are:

Laminar Flow:

$$\frac{C_{f,\ell,0}}{2} = \frac{0.220}{\mathrm{Re}_\Theta}$$

$$C_{h,\ell,0} = \frac{0.220}{\mathrm{Pr}^{4/3}\,\mathrm{Re}_\Phi}$$

Turbulent Flow:

$$\frac{C_{f,t,0}}{2} = \frac{0.245}{\mathrm{Re}_\Theta} + \frac{0.010742\,\mathrm{Re}_\Theta}{100+\mathrm{Re}_\Theta}\left(\log_{10}\mathrm{Re}_\Theta\right)^{-1.5262}$$

$$C_{h,t,0} = \frac{0.22}{\mathrm{Pr}^{4/3}\,\mathrm{Re}_\Phi} + \frac{a\,\mathrm{Re}_\Phi}{\left(100+\mathrm{Re}_\Phi\right)}\left(\log_{10}\mathrm{Re}_\Phi\right)^{-b}$$

For Pr ≥ 0.6,

$$a = 0.0993e^{(0.0648\Pr)} / (1.0 + 9.6\Pr)$$

$$b = 1.954e^{(0.273\Pr)} / (1.0 + 0.71\Pr)$$

and for Pr < 0.6,

$$a = 0.1256e^{(0.2435\Pr)} / (1.0 + 14.2\Pr)$$

$$b = 2.217e^{(0.6313\Pr)} / (1.0 + 1.677\Pr)$$

Boundary Layer Shape and Recovery Factors

Currently, the shape factors employed in MEIT are based on simplistic laws: 1) zero pressure gradient Karman-Polhausen boundary layer profiles for laminar conditions; 2) (1/n) power profiles for the turbulent boundary layer, where n is a function of Re; and, 3) velocity squared total enthalpy distribution through the boundary layers.

The boundary layer recovery factor, *R*, is needed to compute recovery enthalpies for heat transfer and boundary layer reference property evaluations. It is defined as:

$$R \equiv \frac{h_r - h_e}{h_{t,e} - h_e}$$

The expressions used to represent the laminar shape and recovery factors are:

$$H_\ell = 3.029\frac{r_e}{r_w} - 0.614$$

$$F_\ell = 1.521 + 4.388\left(\frac{r_e}{r_w} + 0.0378\right)^{1/2}$$

$$R_\ell = \Pr^{1/2}$$

Additional curve fits for the shape factors H and F in turbulent flow were developed from parametric two-layer boundary layer profile calculations that used Couette flow with mixing length theory for the inner layer and compressible simple wake theory in the outer layer. The recovery factor for turbulent flow is $R_t = \Pr^{1/3}$.

Transitional and Non Ideal Effects

For natural transition, the dependence of the parameters $C_f/2$, C_h, H, F and R (the recovery factor) on the boundary layer state is established via the transitional intermittency factor. This factor is zero in laminar flow, unity in turbulent flow and between 0 and 1 for transitional flow. The transitional intermittency that is employed in ATAC is based on the work of Persh, according to the interpretation of Dahm[5].

Non-ideal effects are modeled through the use of influence coefficients. These coefficients are factors that are derived by comparing the convective transfer with the ideal flat-plate result for the same boundary layer state. These factors are generally derived for only one non-ideal mechanism at a time. The MEIT procedure assumes that the Stanton number, C_h, and the friction factor, $C_f / 2$, can be written as:

$$C_{x,y} = C_{x,y,0} \prod^{z} I_{x,y,z} \text{ for } x = h,\ f \text{ and } y = \ell, t$$

where $C_{x,y,0}$ refers to the basic law for incompressible flow along an impervious, isothermal flat plate, x indicates heat or momentum transfer, y indicates laminar or turbulent flow, and z indicates the non-ideal effect being considered. Current effects modeled in ATAC include acceleration caused by finite pressure gradients, real gas and Mach number effects, surface roughness, and mass transfer. A complete description of these models is given by Murray.[3]

CMA TRANSIENT THERMAL ENVIRONMENT

CMA uses an implicit, finite-difference procedure for computing the one-dimensional transient transport of thermal energy in a material that can ablate from a front surface and decompose in-depth. Figure 3 illustrates the general physical problem treated by CMA. As the material is heated, one or more components of the original composite material pyrolyzes and yields a pyrolysis gas and a porous residue. The pyrolysis gas percolates away from the pyrolysis zone. The residue, for many materials of interest, is a carbonaceous char possibly reinforced with refractory fibers or cloth.

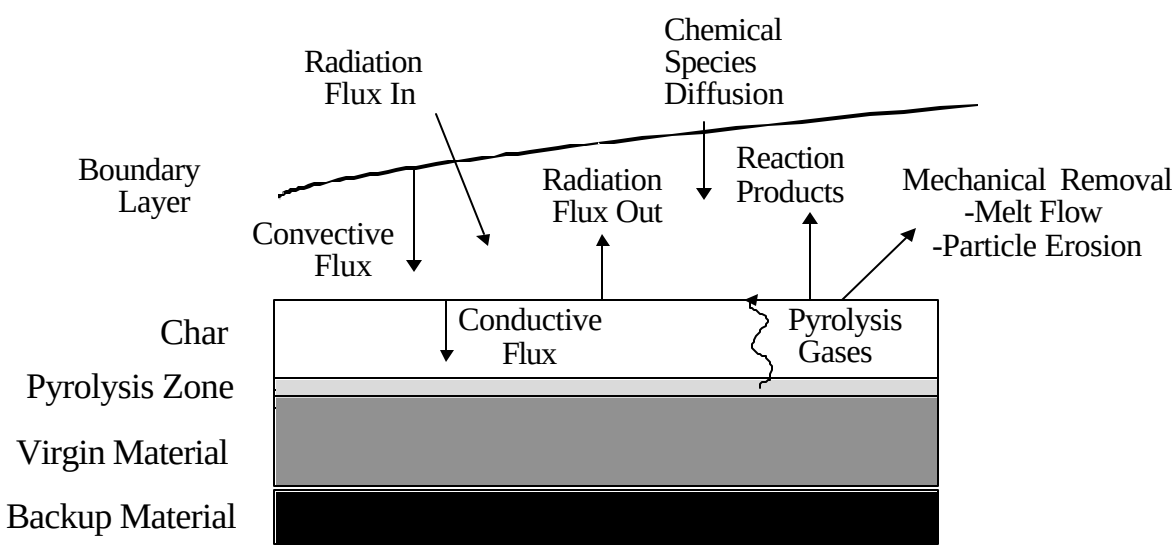

Figure 3: Schematic of the general surface energy balance

The in-depth solution procedure is basically a transient heat conduction calculation coupled to a pyrolysis rate calculation and to boundary conditions from the flowfield solution. The coupling with the boundary conditions is provided through a surface energy balance solution.

DECOMPOSITION (PYROLYSIS OR CHARRING)

Since many decomposing materials appear to behave as three independently pyrolyzing components, the program uses a three-component decomposition model for the surface materials and for any decomposing back-up materials. The resin filler is presumed to consist of two components that decompose separately, while the reinforcing material is the third component that can also decompose. The instantaneous density of the composite is given by:

$$r = \Gamma\left(r_A + r_B\right) + \left(1 - \Gamma\right) r_C$$

where A and B represent components of the resin and C represents the reinforcing material, and Γ is the volume fraction of the resin. Each of the three components can decompose following the relation:

$$\left.\frac{\partial r_i}{\partial q}\right|_x = -B_i \exp\left(\frac{-E_{a_i}}{RT}\right) r_{o_i} \left(\frac{r_i - r_{r_i}}{r_{o_i}}\right)^{j_i}$$

where r_{r_i} is the residual density and r_{o_i} is the original density of component i. The values B_i, j_i, and E_{a_i} along with the above densities are input parameters for each of the three components of the surface material. A separate set of pyrolysis data may be entered for each decomposing back-up material.

IN-DEPTH THERMAL SOLUTION

The in-depth energy balance equation is written in a coordinate system tied to the receding surface, as shown in Fig. 4. In this system, the equation becomes:

$$r\, c_p \left.\frac{\partial T}{\partial q}\right|_z = \frac{1}{A}\frac{\partial}{\partial z}\left(kA\frac{\partial T}{\partial z}\right)_q + \left(h_g - \bar{h}\right)\left.\frac{\partial r}{\partial q}\right|_x + \dot{s}\, r\, c_p \left.\frac{\partial T}{\partial z}\right|_q + \left.\frac{\dot{m}_g}{A}\frac{\partial h_g}{\partial z}\right|_q$$

in which the individual terms represent the rate of sensible energy storage, the net rate of thermal conduction, pyrolysis energy rate, convection rate of sensible energy due to coordinate system movement, and the net rate of energy convected with the pyrolysis gas.

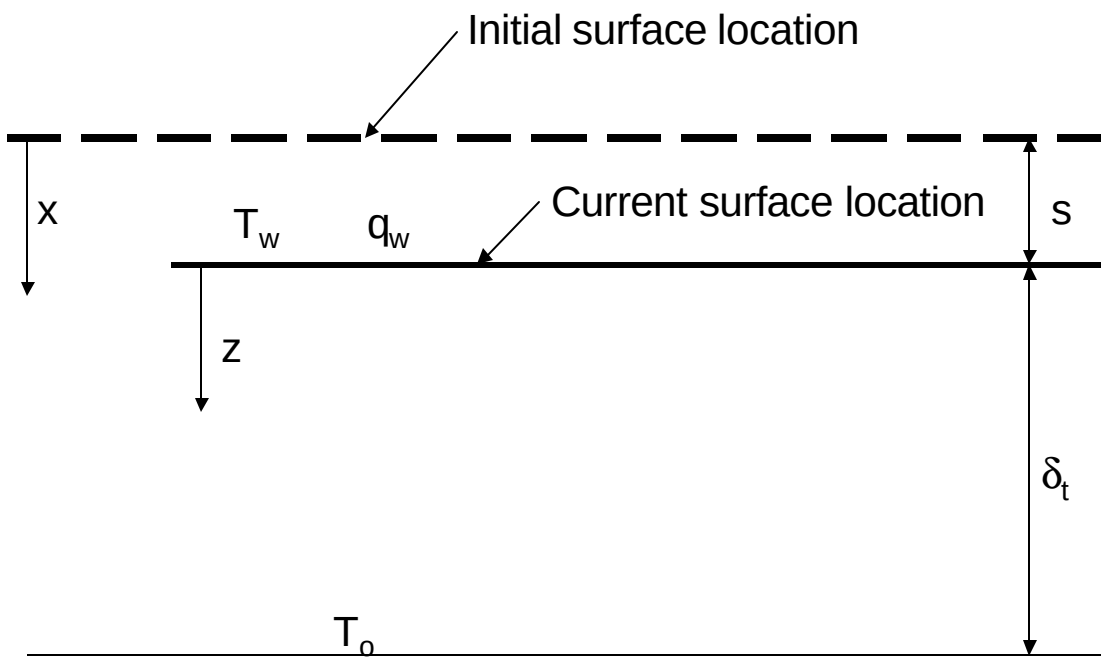

Figure 4: Coordinate System for the In-depth Thermal Solution

The internal energy equation is computed implicitly for each node, using new temperatures in the heat conduction terms. The energy balance is linked explicitly to the decomposition events, since the pyrolysis gas fluxes are derived from the explicit decomposition calculation. The energy equation is also linked explicitly to the surface boundary condition through the use of the old recession rate in all convection terms involving the fluxes of solids. All other links to the surface events are implicit.

The implicit formulation of the in-depth nodal energy equations yields a tri-diagonal set of equations that is solved for the unknown temperatures in two passes of direct elimination. The first pass eliminates one unknown from each equation and leaves the equation for the first node with only one unknown, the surface temperature. This unknown temperature is solved using an iterative procedure in the surface energy balance. Once this temperature is determined, the second elimination pass determines the other unknown nodal temperatures at each of the in-depth nodes.

GENERAL SURFACE ENERGY BALANCE

The events at the heated surface are determined by convective heating and by the surface thermochemical interactions with the boundary layer gases. Figure 3 illustrates the energy fluxes of interest at the surface. The surface energy balance equation employed is of the convective transfer coefficient type. This energy balance equation takes the following form:

$$r_e u_e C_H \left(h_r - h_{e_w}\right) + r_e u_e C_M \left[\sum_i \left(Z_{i_e}^* - Z_{i_w}^*\right) h_i^{T_w} - B' h_w \right] + \dot{m}_c h_c + \dot{m}_g h_g + a_w q_{rad} - F s\, e_w T_w^4 - q_{cond} = 0$$

The energy fluxes described in the above equation represent the sensible convective heat flux, the chemical energy flux, the fluxes entering the control volume from within the solid material, the net radiative heat flux, and the energy conducted into the body. From the first pass of the tri-diagonal reduction of the in-depth solution, the conduction term can be expressed as:

$$q_{cond} = AT_w + B$$

This expression may be substituted into the surface energy balance and yields a non-linear equation in T_w that is solved iteratively by a Newton-Raphson method.

RESULTS

Calculations have been done for three test cases to demonstrate the capabilities of the code. These test cases are for very blunt reentry vehicles such as the Apollo capsule and the Pascal Entry, Descent and Landing (EDL) Module. The first case is wind tunnel tests on a scale model of the Apollo capsule. Pressure and heat flux measurements were taken in Mach 9 flow at JPL and in Mach 10 at AEDC. A second series of measurements was taken at Langley in Mach 20 flow with helium. The second case is a flight prediction for the Apollo re-entry. Thermocouples were used to measure the temperature response within the Apollo heatshield material. The third case is the design of the Pascal EDL module where ATAC was used to calculate aerodynamic coefficients of the module throughout a Martian entry.

APOLLO WIND TUNNEL TESTS

Surface pressure and heat flux distributions on a sub-scale model of the Apollo capsule are presented in Refs. 11 and 12. The Apollo capsule is a very blunt configuration and these comparisons demonstrate the code's ability to predict the surface pressure on blunt vehicles. These two tests were also done in two different gases. Bertin's[11] tests were done in air at Mach 9 while Marvin's[12] tests were conducted in helium at Mach 20. Figure 5 presents the ATAC geometry model for the Apollo capsule. The flat facets that are seen in the figure on the left are a result of the plotting increments used to output the surface. The actual geometry is continuous across all of these plot increments. Using a finer plot increment would produce a smoother surface as shown in the figure on the right. Figure 6 compares the ATAC pressure prediction with data for Bertin's report at α=0 deg. The distribution is in excellent agreement with the measurements. Figure 7 compares the heat flux distribution with data in air at Mach 10. ATAC overpredicts the heat flux at the corners of the vehicle where the pressure gradients are very large but overall the agreement is very good. Figure 8 shows the predicted pressure distribution in helium compared with data from Martin. This calculation required a new set of gas properties in ATAC and exercised the new Mollier option in the code. This option allows the user to input a Mollier table for different gases instead of using the air tables that were built into the original code. Again the agreement with the experimental data is excellent. Figure 9 presents the heat flux distribution in helium. ATAC overpredicts the flow around the corner but the agreement on the heatshield is still reasonable. Figures 10 and 11 present the pressure and heat flux distributions at Mach 20 in helium but at 25 degrees angle of attack. The predictions are in reasonable agreement with the data considering the complexity of the flow and the proximity of the stagnation point to the corner.

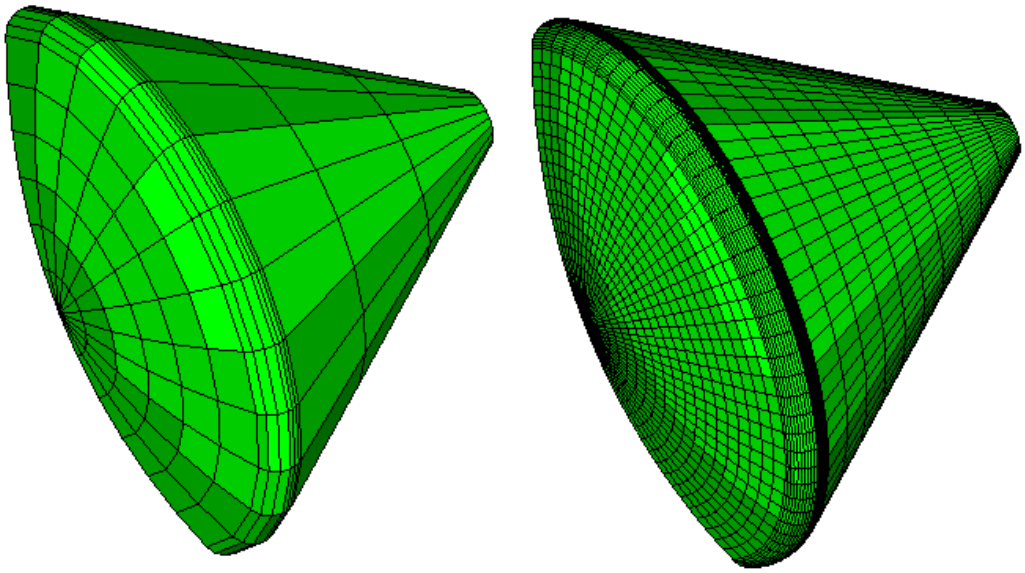

Figure 5: ATAC Surface Geometry for the Apollo Capsule

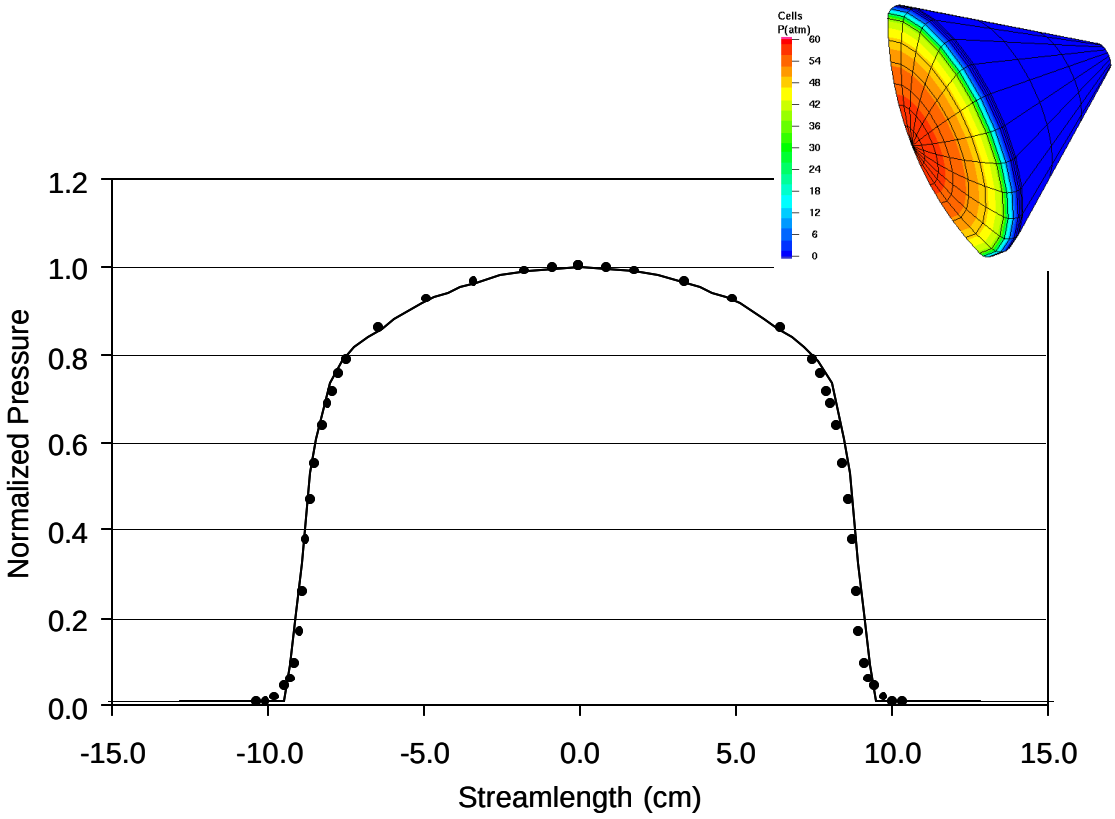

Figure 6: Comparison with Pressure Data at Mach 9 in Air, a **=0**

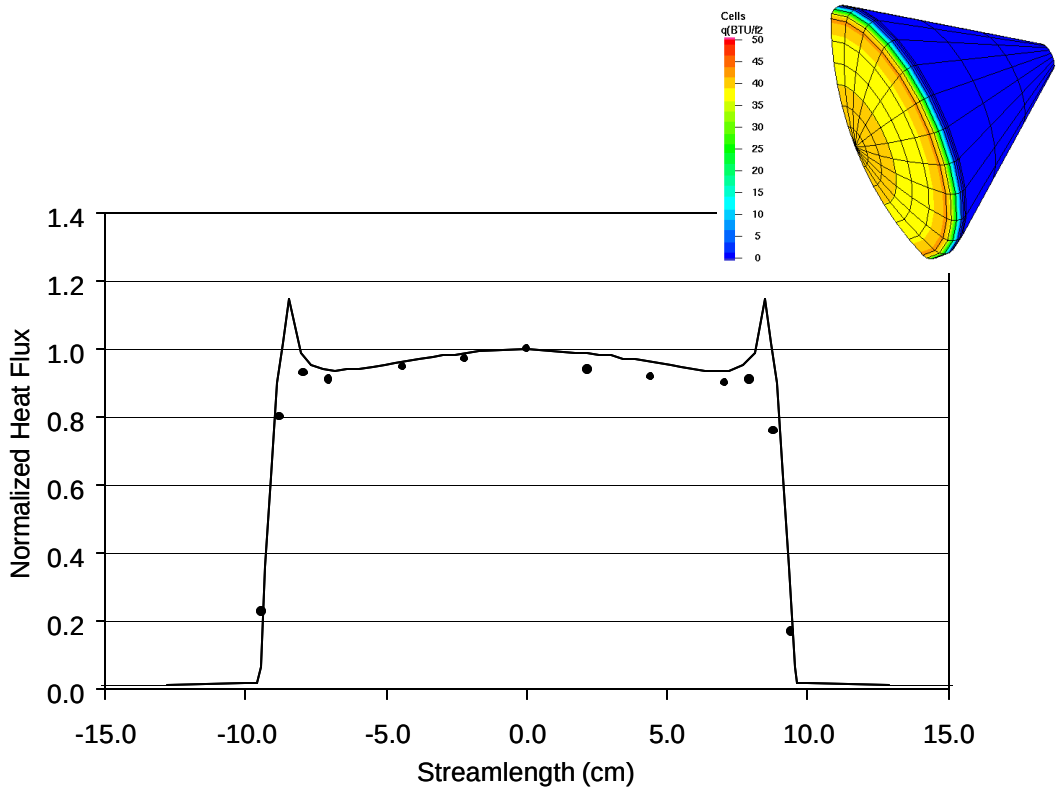

Figure 7: Comparison with Heat Flux Data at Mach 10 in Air, a **=0**

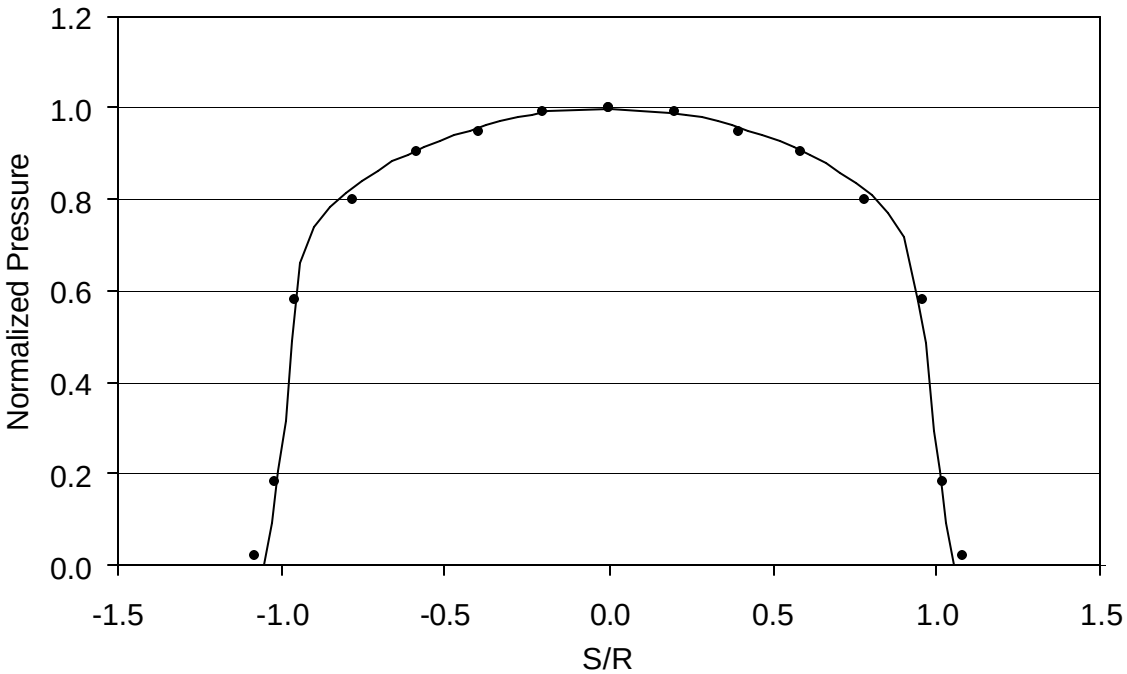

Figure 8: Comparison with Pressure Data at Mach 20 in Helium, a **=0**

Figure 12 compares ATAC heat flux predictions with those from BLIMP[13] and from a compilation of data by the Johnson Space Center (JSC) at an angle of attack of 25 degrees. The heat flux on the upper part of the heatshield is underpredicted by ATAC. This is also seen in Figure 11 where the heat flux around the stagnation point is lower than the data. On the windward side, the stagnation point velocity gradient predicted by ATAC creates a large increase in the heat flux and the heating on the corner is overpredicted. Some of this is due to the step size taken by the streamline tracing over the windward side. The first point away from the stagnation point is almost a quarter of the nose radius and can be seen in Fig. 11 as the linear portion of the curve between s/R_n=0.72 and 1.0. This large step makes it impossible for the stagnation heating logic to obtain a good solution.

APOLLO REENTRY FLIGHT

Post flight analysis of the Apollo heatshield performance has been documented in Ref. 13. During this work, improvements were made in the Boundary Layer Integral Matrix Procedure (BLIMP) and CMA to model the coking phenomena in the Avcoat 5026-39/HC-GP ablator that formed the heatshield of the Apollo capsule. Comparisons were made with thermocouple measurements, char depth measurements and char density measurements throughout several Apollo flights. For the present work, comparisons were made with Flight 202. This was a relatively nonsevere convective heating environment with negligible radiation heating and almost no recession. Since the version of CMA that was incorporated in ATAC does not have the coking model, this flight would be a better comparison with ATAC than the more severe cases where coking was larger factor in the thermal analysis.

Trajectory information was taken from the Postlaunch Report[14] and is shown in Figure 13. The calculation was started at 360,000 feet with a nominal angle of attack of 18.75 degrees. The surface material model used the data provided in Reference 13 without the coking or surface recession effects. Comparisons are made with thermocouple data at three locations. All of these were on the plane of symmetry and are shown in Figure 14. The most severe heating was at the z=71 in location. This was near the stagnation point and experienced the highest heating throughout the flight. The second point was on the axis of symmetry and the third was at z=-71 in which on the opposite end from the stagnation point. These three points represent the highest, mid-range and lowest heating points on the heatshield.

Comparisons with the Apollo thermocouple data and with BLIMP/CMAC predictions at the z=71 in location are shown in Fig. 15. Both BLIMP/CMAC and ATAC were in reasonable agreement with the data at the 0.05 depth. Both procedures overpredicted the response in the first 150 seconds. The CMAC calculation predicted that the surface would recede past the 0.05 in thermocouple at 4850 sec and the solution stopped at that point. At the 0.35 in thermocouple, ATAC was in better agreement up to 4750 seconds when the thermocouple data began to increase and approached the values predicted by CMAC. This may be due to the start of coking in the char layer. The z=0.0 in location is shown in Figure 16. The results at this station were similar to those at z=0.71 in.

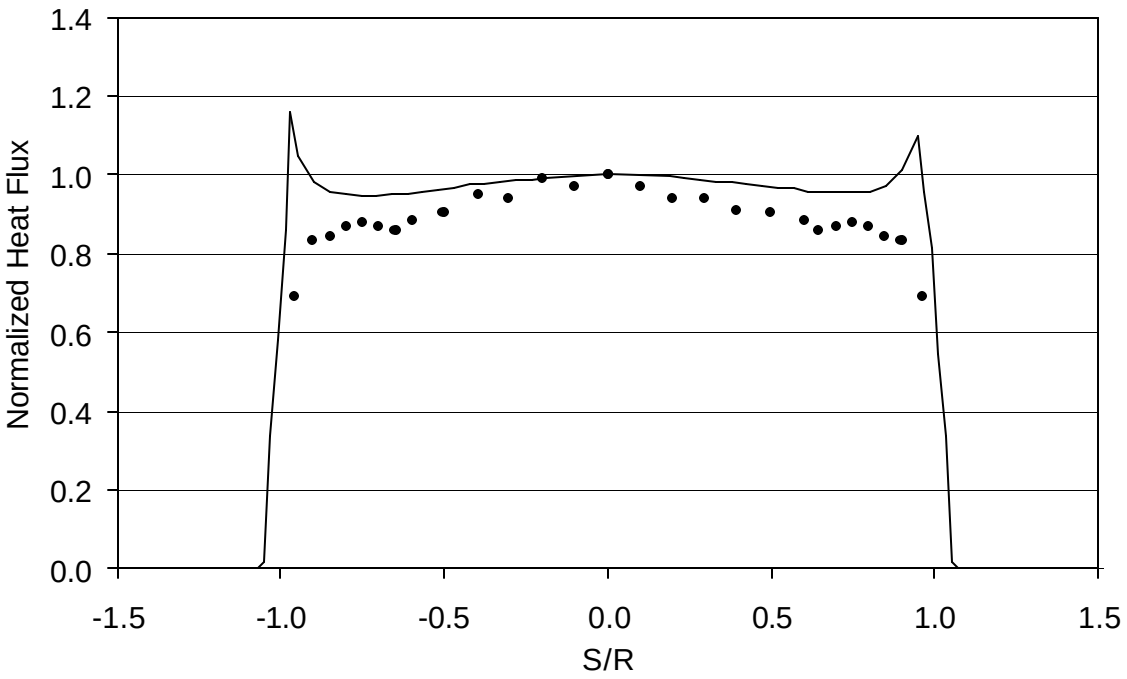

Figure 9: Comparison with Heat Flux Data at Mach 20 in Helium, a **=0**

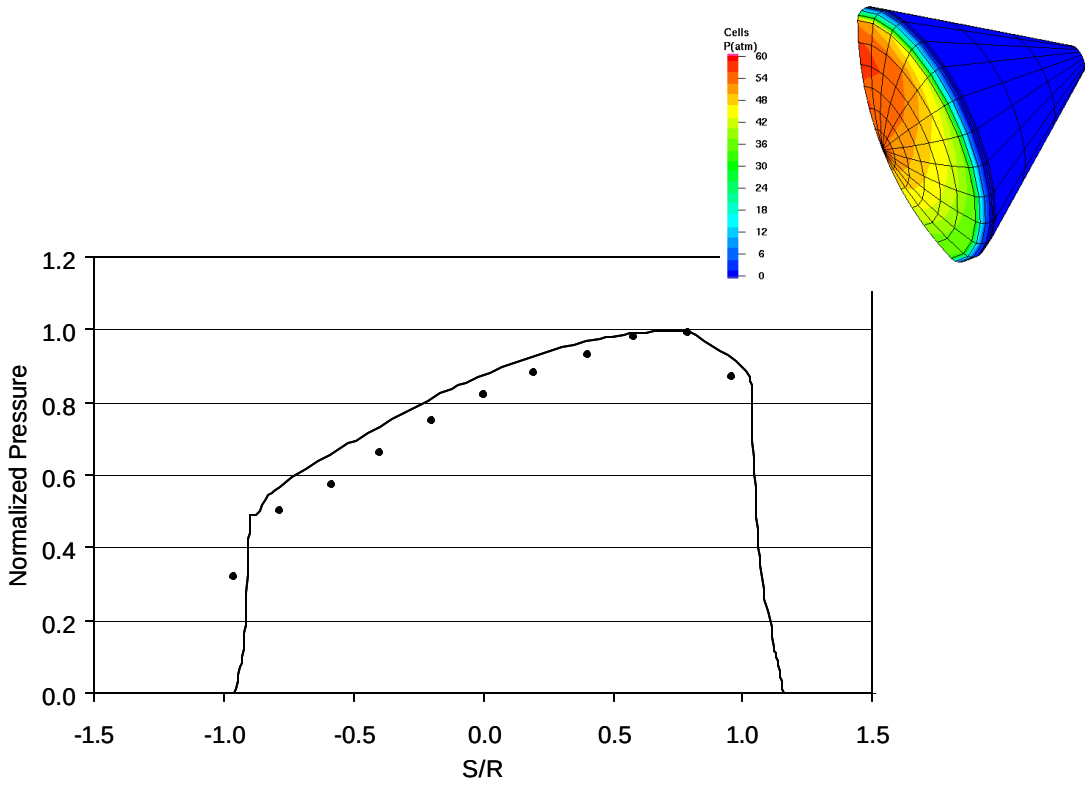

Figure 10: Comparison with Pressure Data at Mach 20 in Helium, a **=25 deg**

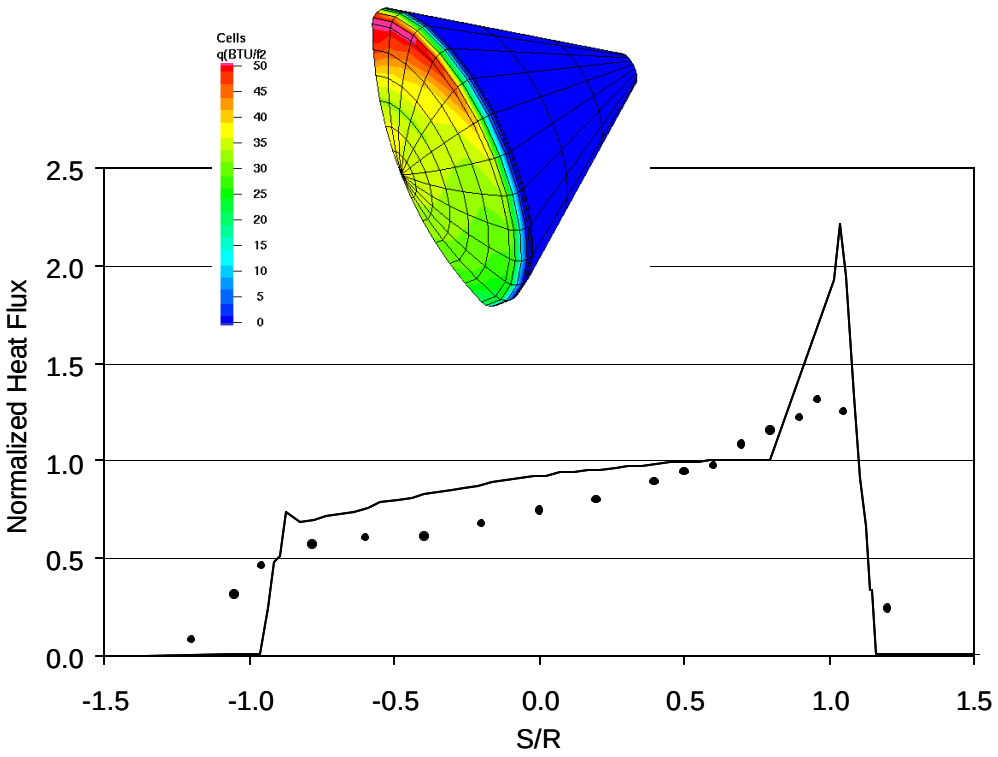

Figure 11: Comparison with Heat Flux Data at Mach 20 in Helium, a **=25**

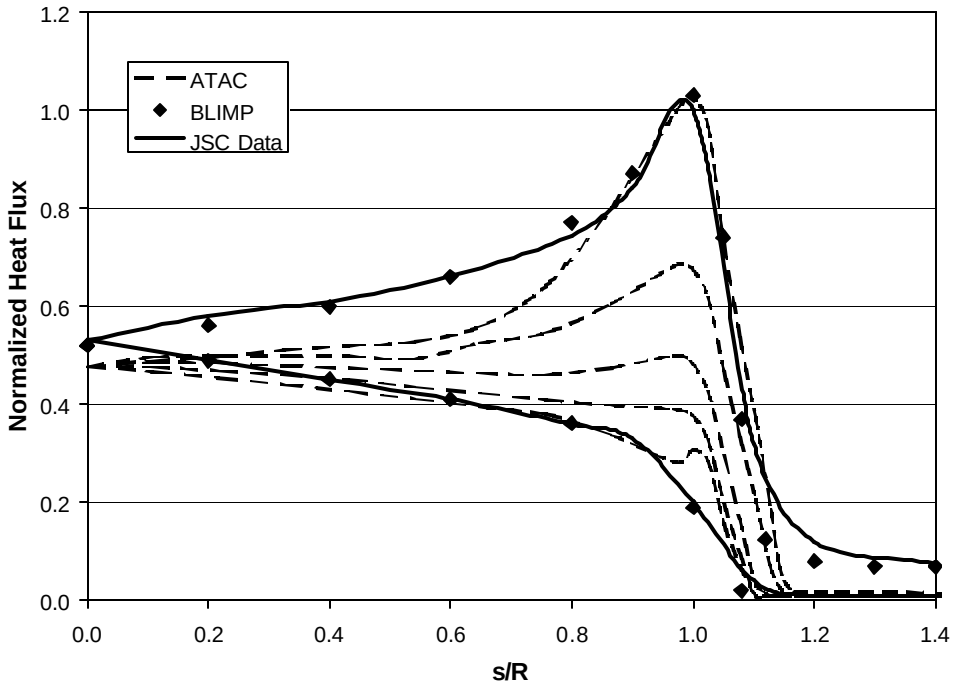

Figure 12: ATAC Comparisons with BLIMP Predictions and JSC Data at a **=25**

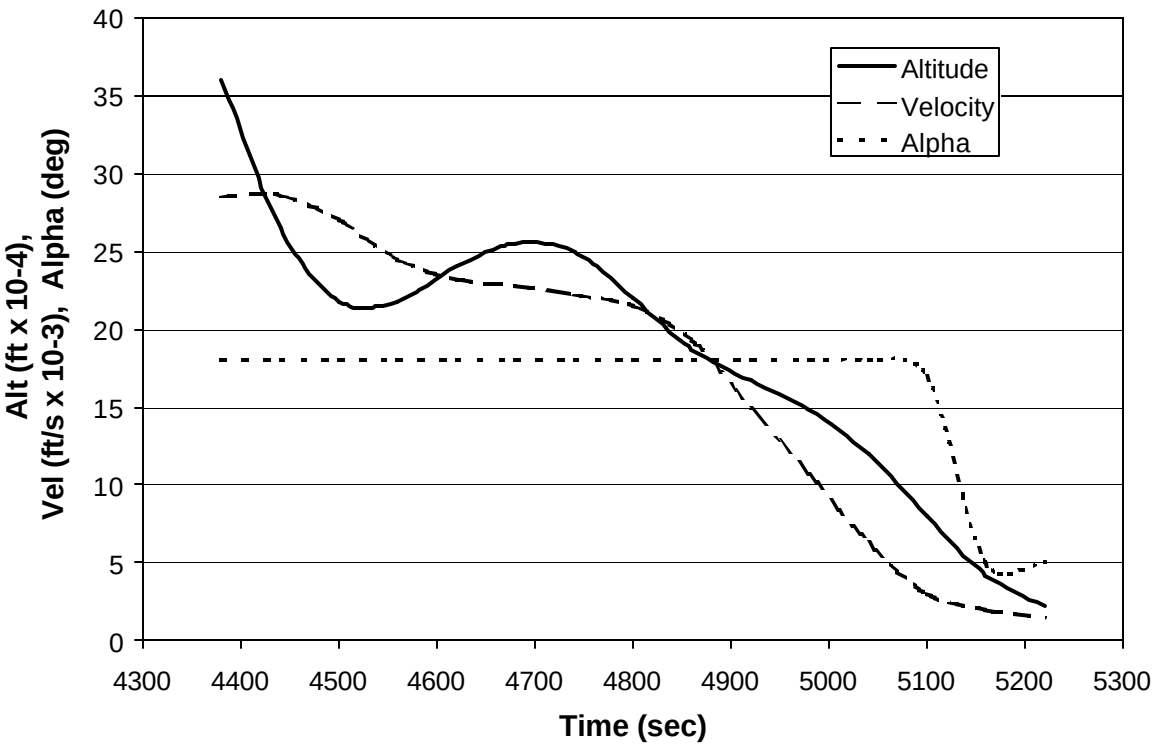

Figure 13: Flight 202 Trajectory Parameter

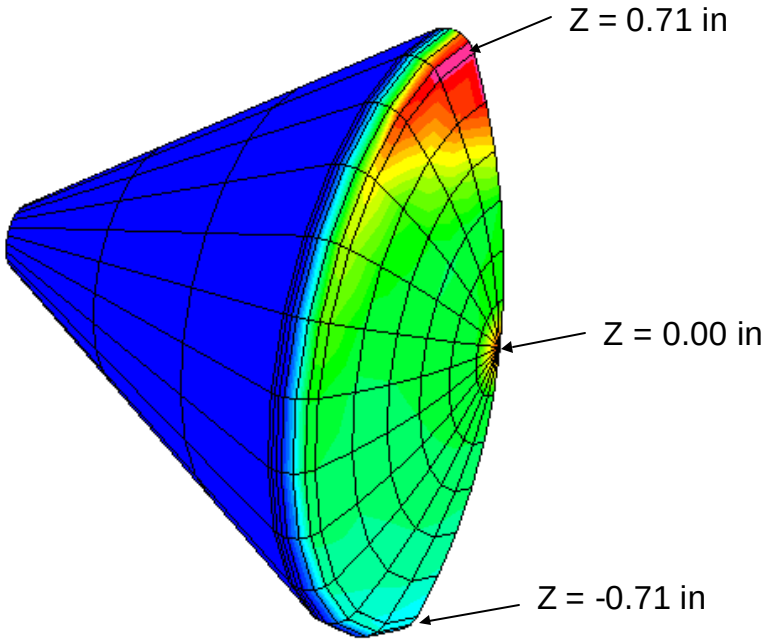

Figure 14: Thermocouple Locations on Apollo Flight 202

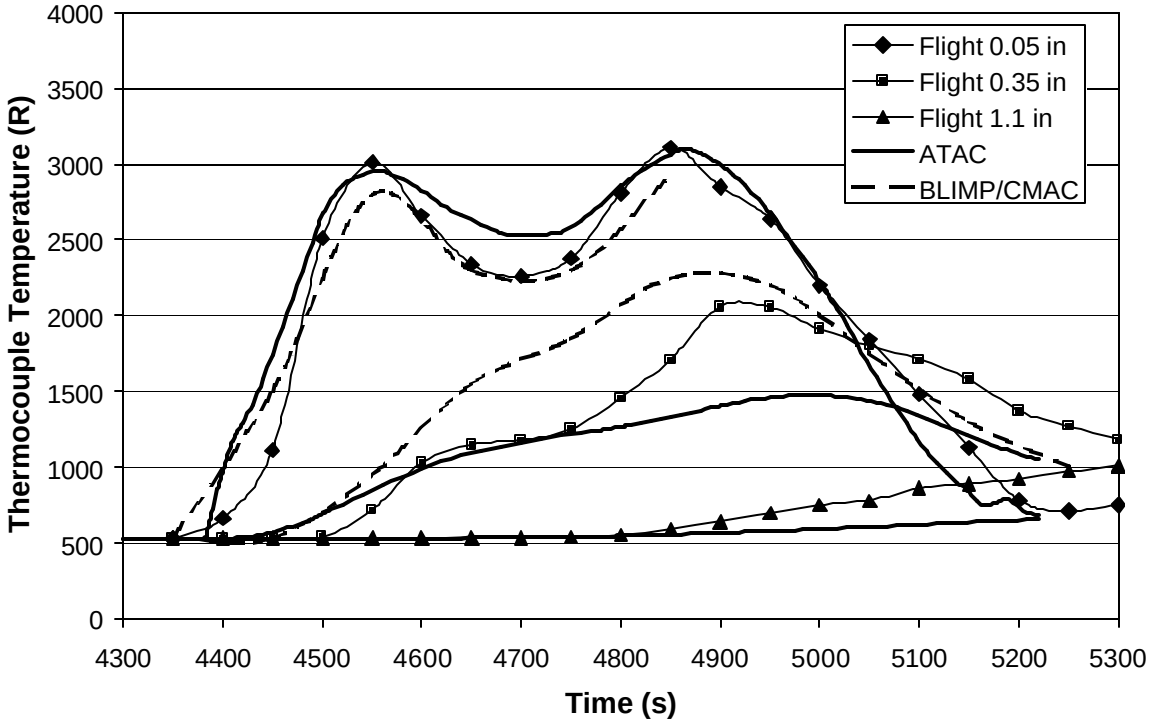

Figure 15: Comparisons with Thermocouple Data at z=71 in

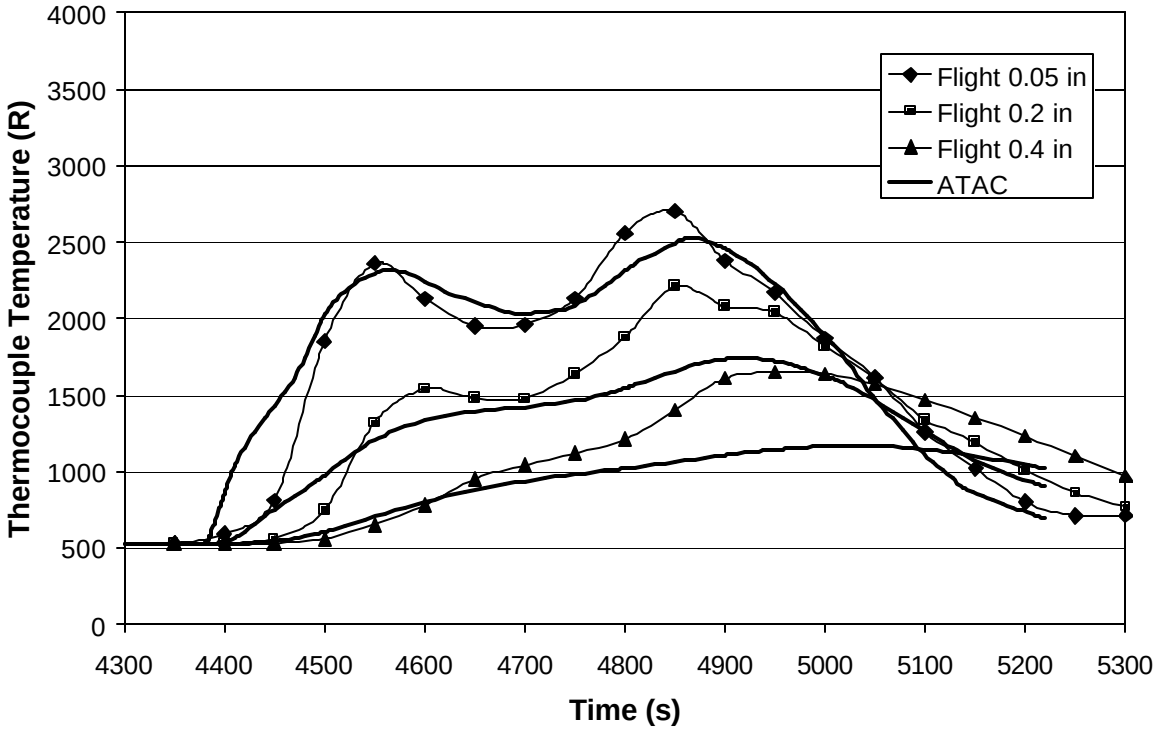

Figure 16: Comparison with Thermocouple Data a z=0 in

ATAC overpredicted the initial response at 4400 sec but did a reasonable job at the 0.05 in thermocouple. At the 0.2 and 0.4 in depths, the agreement was good up to 4750 seconds and then the thermocouple data showed an increase that ATAC did not predict. The peak temperatures at this location were about 500 R cooler than at z=71 in. The z=-71in results are shown in Figure 17 and follow the same trend as the other two stations. Again the peak temperatures are about 500 R lower than at z=0 in since this is one of the cooler locations on the heatshield.

Figure 18 presents comparisons of the char depth with the CMAC predictions and with char sensor data from Flight 202. The onset of char is determined by the location where the surface material has lost 2% of its original density. The material decomposes very rapidly after char onset. The pyrolysis region is between 0.05 and 0.2 inches thick throughout the flight. The predictions of the char depth show the same trends as the thermocouple data. ATAC agrees well with the data up to 4800 seconds but the predicted progression of the pyrolysis region slows down after this time while the data shows an increase in the rate.

Temperature and density profiles at the z=0.71 in location are shown in Figures 19 through 21. Figure 19 presents the temperature profiles through the surface material at flight times of 4500, 4700, 5000, and 5220 seconds. The 4500-second profile corresponds to the first heating peak in the flight. At 4700 seconds, the heating has decreased somewhat due to the increase in the altitude. The 5000-second profile is during the cooling as the capsule slows down in the denser air and the 5220-second profile is at the end of the trajectory data. From the profiles in Figure 19, the cooling that occurs after 5000 seconds is clearly visible and the surface has cooled completely by the end of the trajectory data.

The density profiles through the surface material are shown in Figure 20 at the same times in the flight. At 4500 seconds, the pyrolysis region lies between 0.05 and 0.09 inches. At 4700 seconds, the pyrolysis region is between 0.2 and 0.35 inches. The high heat flux of the first heating peak is driving the decomposition. At 5000 seconds, the pyrolysis region is between 0.3 and 0.5 inches. The heating is less between 4600 and 4800 seconds as the capsule's flight carries it to higher altitudes. The pyrolysis zone stops its recession into the surface material after 5000 seconds. Figure 21 compares the predicted recession with the core measurements from the flight. The ATAC predicted char depth was only half of the flight measurement. The CMAC value was in much better agreement with the flight measurements. This difference may be due to the coking phenomena. The increase in the density profile near the surface of the CMAC prediction is the result of the coking phenomena. This increase in density and conductivity would increase the conduction of the energy into the surface.

PASCAL ENTRY MODULE

The Pascal Program was a proposed Mars SCOUT Program to measure the thermal structure of the atmosphere. A network of up to 24 weather stations was to be placed on the Martian surface to take hourly measurements of the pressure, temperature, humidity and optical depth for 10 Martian years. ATAC was used in the design of the EDL module that was to place the stations on the surface of the planet. The Martian atmosphere is primarily carbon dioxide and a Mollier table was developed for ATAC that would provide the thermodynamic state of the atmospheric gases.

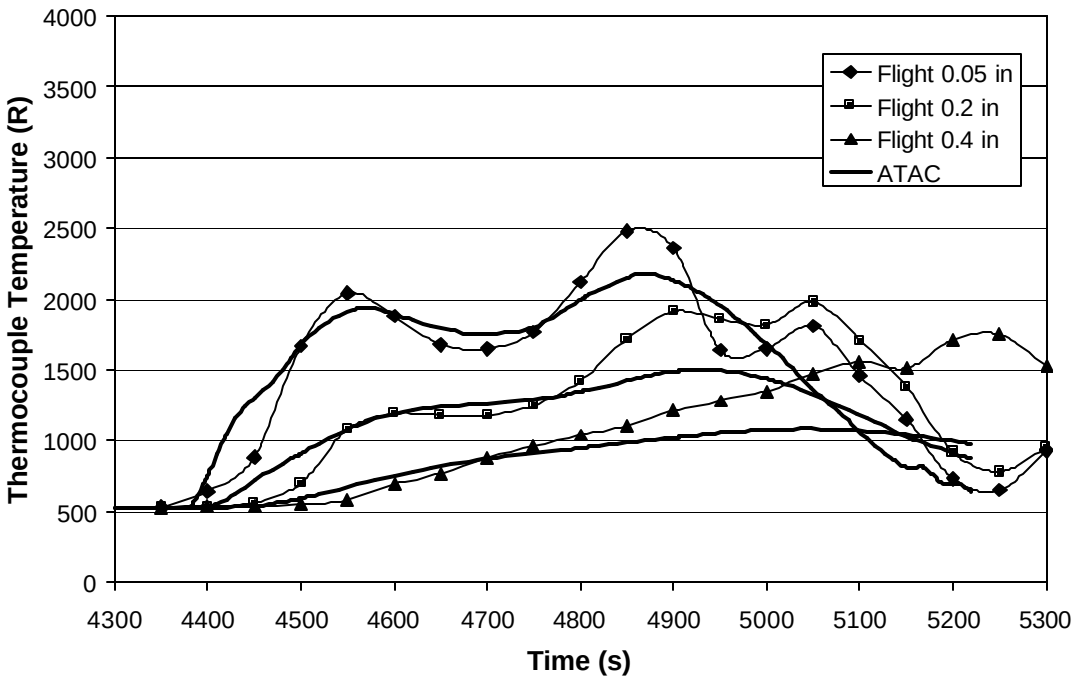

Figure 17: Comparison with Thermocouple Data at z=-71 in

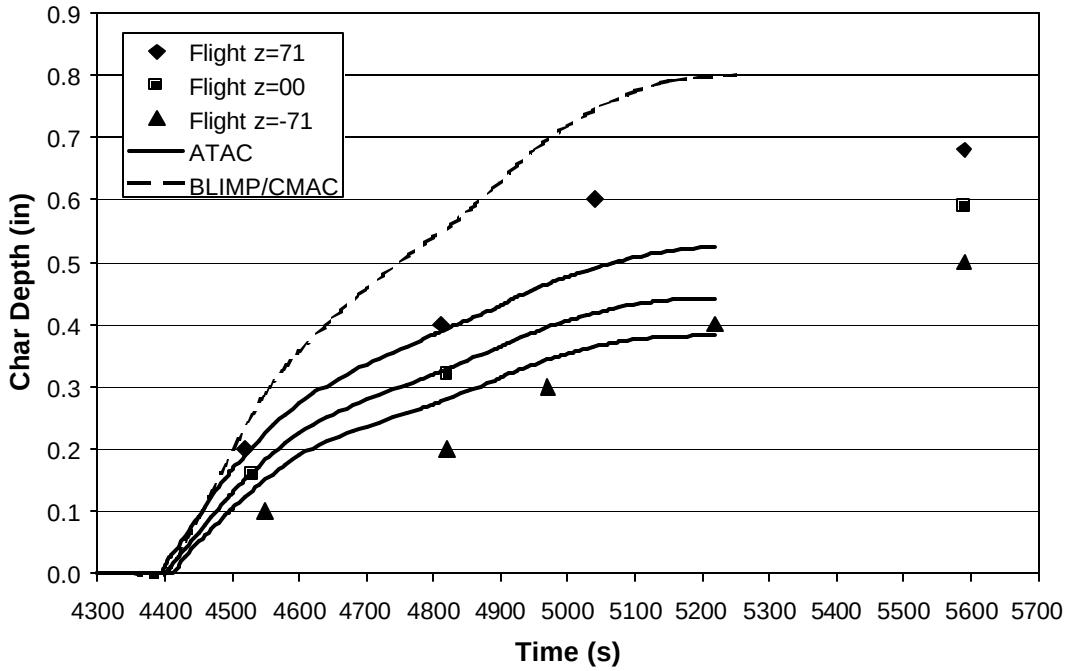

Figure 18: Char Depth Comparisons with Flight Data

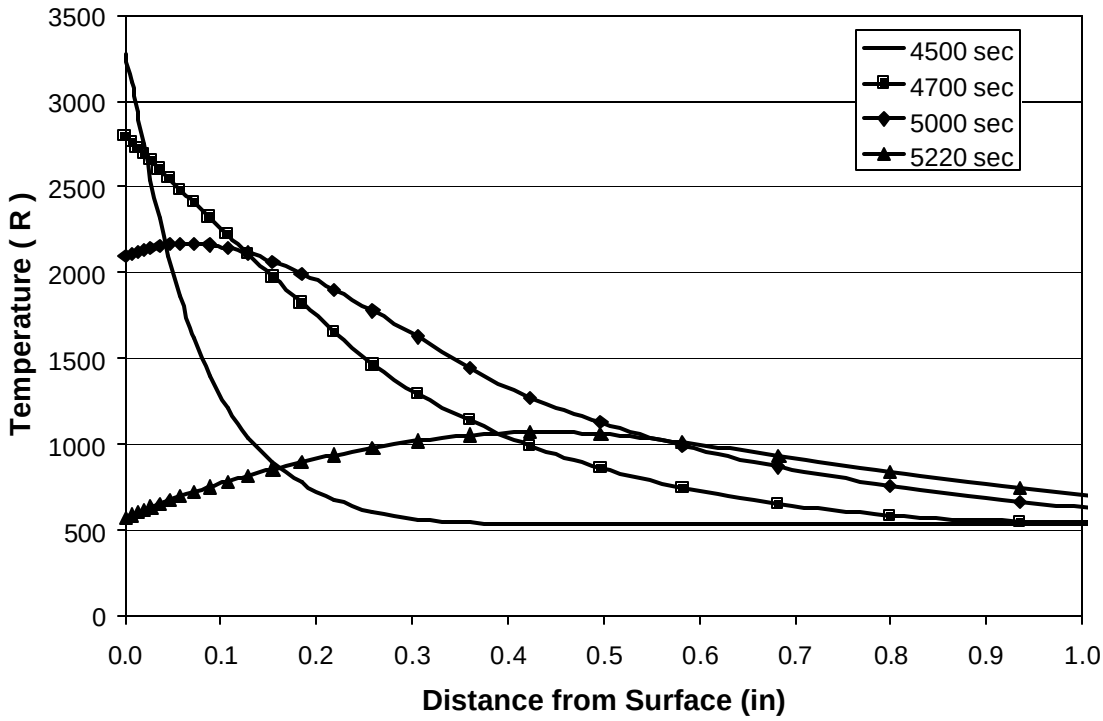

Figure 19: Temperature Profiles in the Surface Material at z=71 in

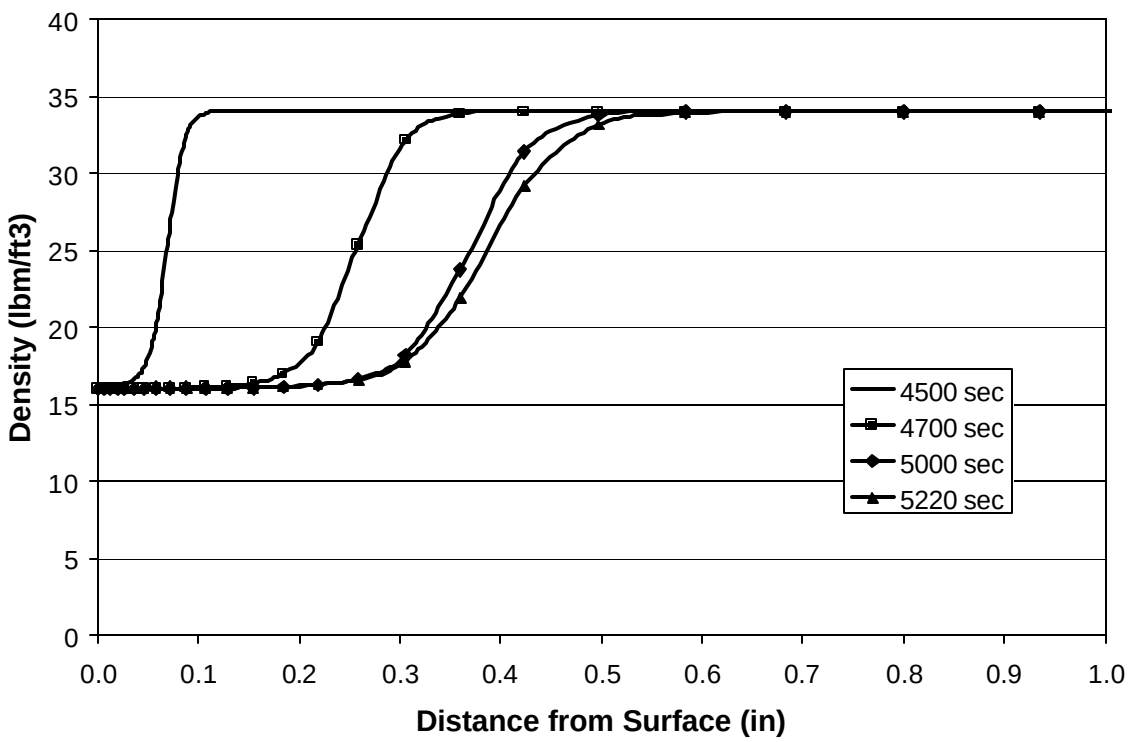

Figure 20: Density Profiles in the Surface Material at z=71 in

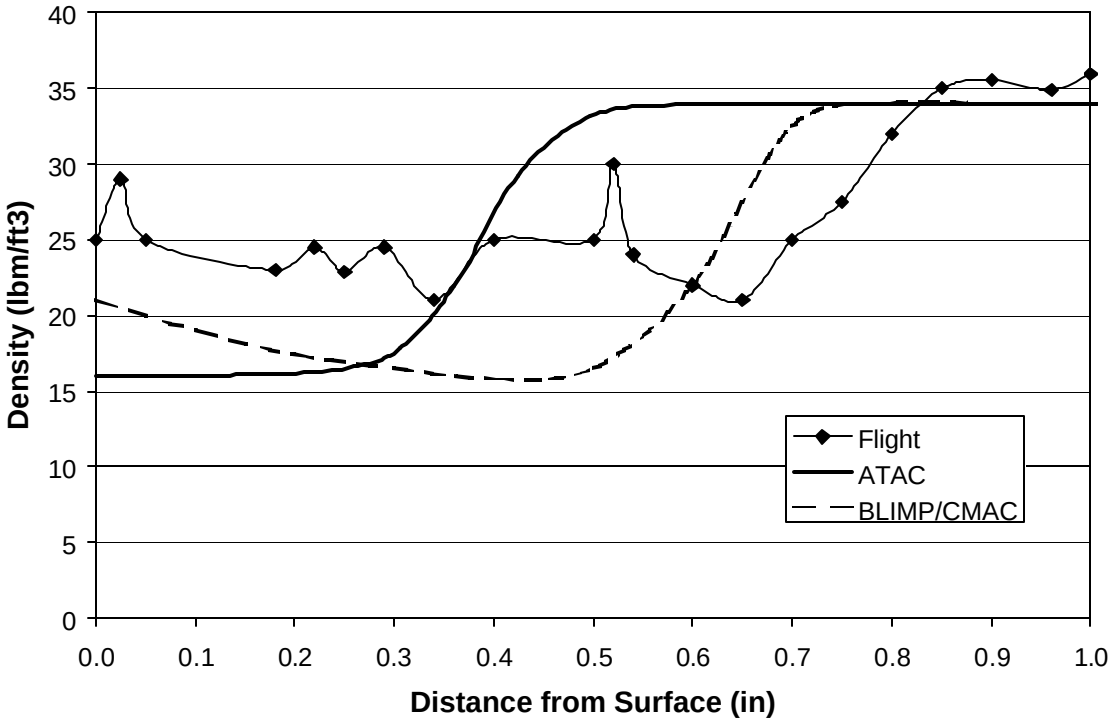

Figure 21: Comparison of Density Profiles with Data from Flight 202

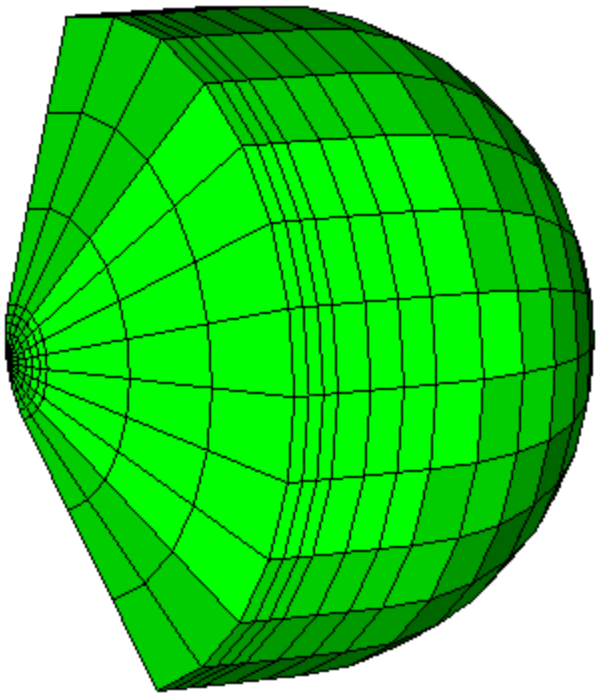

Figure 22: Proposed EDL Module for the Pascal Program

The geometry of the proposed EDL module is shown in Fig. 22. The module consists of a 70-degree forecone and an overall diameter of 19.68 inches. The nose radius on the heatshield was 4.92 inches and the corner radius at the edge of the heatshield was only 0.5 inches. A 4.92-inch cylindrical section followed the heatshield and the aft end was closed with a sphere with a radius of 9.84 inches. ATAC was first used to evaluate the aerodynamic coefficients on the EDL module in the Martian atmosphere. Comparisons were done to verify the drag prediction of ATAC on this configuration. Figure 23 presents the ATAC predictions and comparisons with other analysis. The trajectory simulation began at 115 km where the flowfield was modeled as free molecular (FM) flow. Continuum flow conditions were determined to start at 45.72 km. The ATAC flowfield models allow for bridging between free molecular and continuum flows and the predictions are shown in this figure. Predictions by Ball Aerospace are also shown and are in reasonable agreement with the ATAC bridging. Ball's continuum prediction did not include viscous effects so the drag due to the wall shear is not included. The ATAC solution integrates both pressure and wall shear to determine the drag on the vehicle. Also included in Figure 23 are CFD predictions by Mike Wright of ELORET. The ATAC predictions are in good agreement with these CFD values.

Since the trajectory for the Martian entry had not been determined, the flight analysis was done using the 3 DOF trajectory option in ATAC. The option uses the integrated forces on the vehicle as input into a Runge-Kutta trajectory solution to determine the flight parameters. Figures 24 and 25 compare the predicted ATAC trajectory with a 6 DOF analysis that used a constant drag coefficient of 1.5. The parameters for this trajectory were an entry velocity V=7 km/s and an entry angle of –22 degrees. This was one of the most severe heating trajectories considered in the analysis. The agreement is quite good considering the difference in the drag coefficients. Figure 26 presents the predicted ATAC drag coefficient as a function of the altitude and compares it with the constant 1.5 value used in the 6 DOF code. The predicted drag coefficient is always larger than 1.5. It starts as high as 2.5 in the free molecular region and decreases to about 1.75 at 20 km.

The distributions of pressure and heat flux over the EDL vehicle are shown in Figures 27 and 28. These distributions are shown at the maximum pressure point and the maximum heating point in the trajectory. The maximum pressure occurs at 19000 m and the maximum heating occurs at 28000 m. The pressure is reasonably constant over the blunt heatshield. On the side wall the pressure drops by a factor of 20 but remains fairly constant. On the aft closure the pressure continues to drop until it reaches the freestream pressure. The heat flux is not constant over the heatshield but shows a large drop from the stagnation point. Near the corner, the heat flux increases at the peak heating condition by continues to decrease for the peak pressure. On the aft closure, the heat flux is almost negligible. Figure 29 presents the predicted wall temperature for the peak heating and peak pressure time. These temperatures are for a heatshield made of Acusil 2. The surface temperatures are over 2500 K at the stagnation point and over 1200 K even on the sidewall.

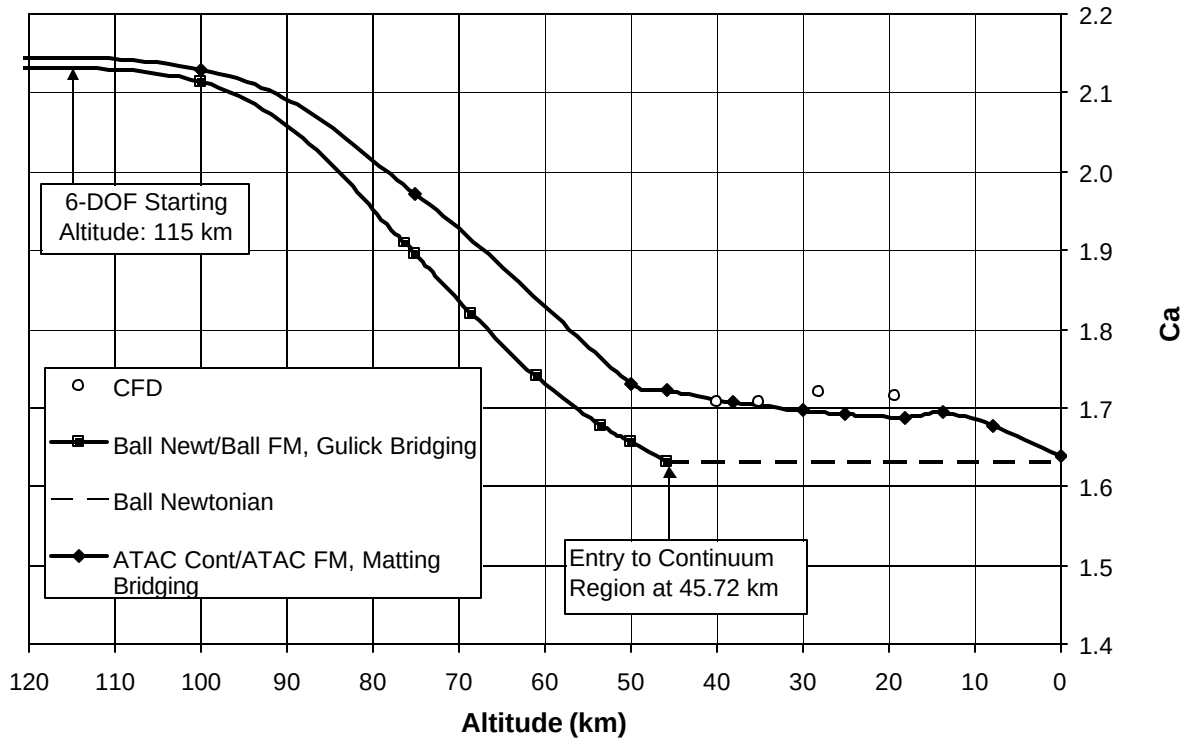

Figure 23: ATAC Drag Predictions for the Pascal EDL

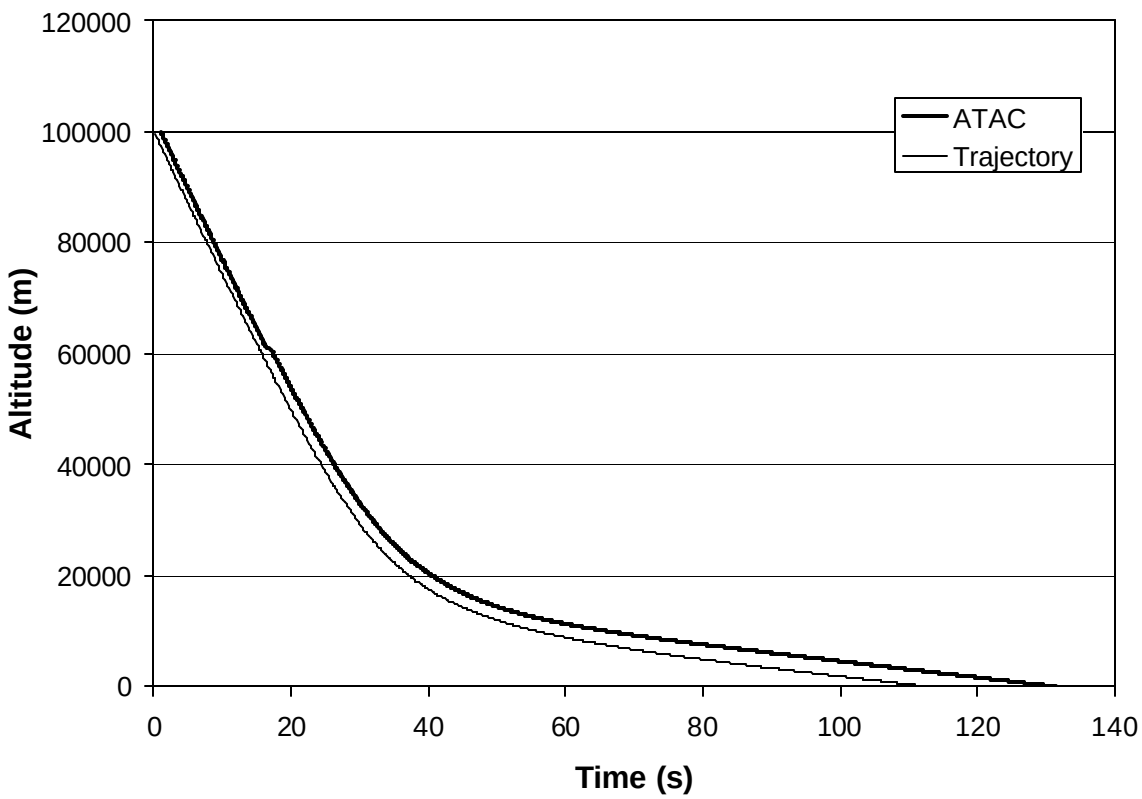

Figure 24: Altitude vs. Time for the V=7 km/s, g=-22 Trajectory

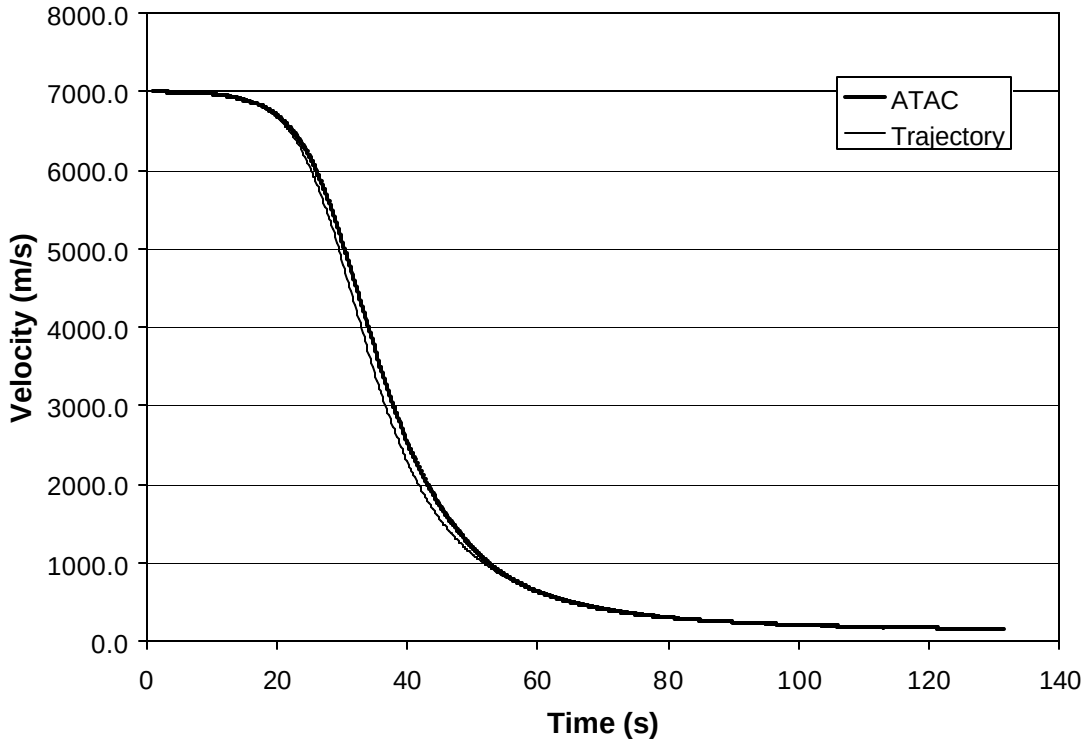

Figure 25: Velocity vs. Time for the V=7 km/s, g=-22 Trajectory

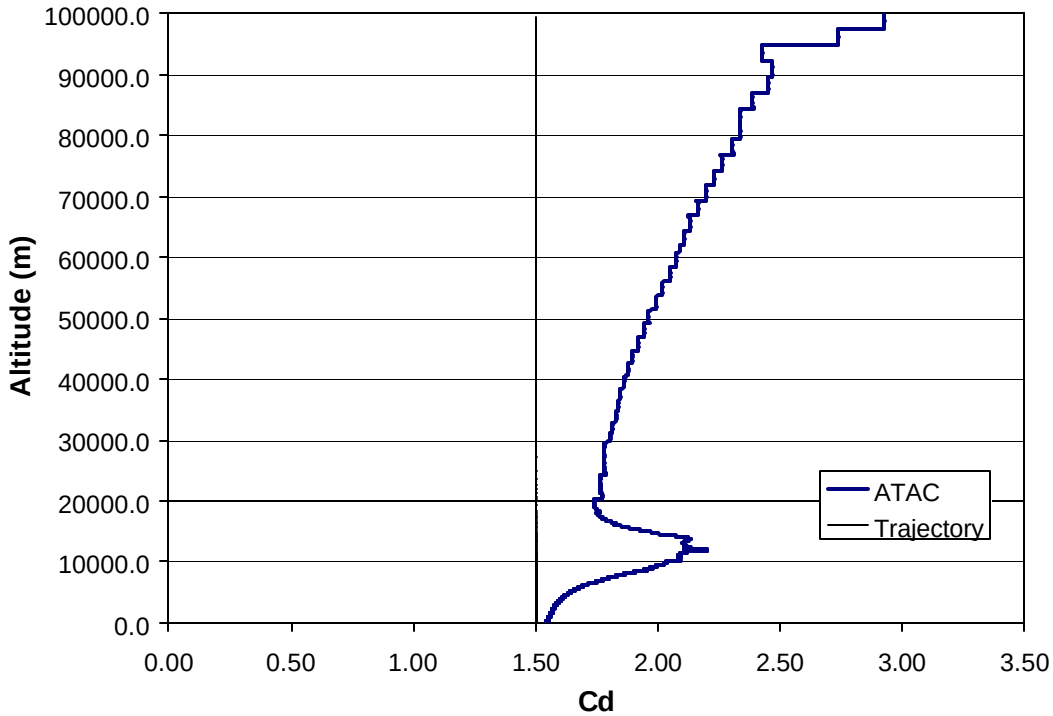

Figure 26: Drag Coefficient vs. Altitude for the V=7 km/s, g=-22 Trajectory

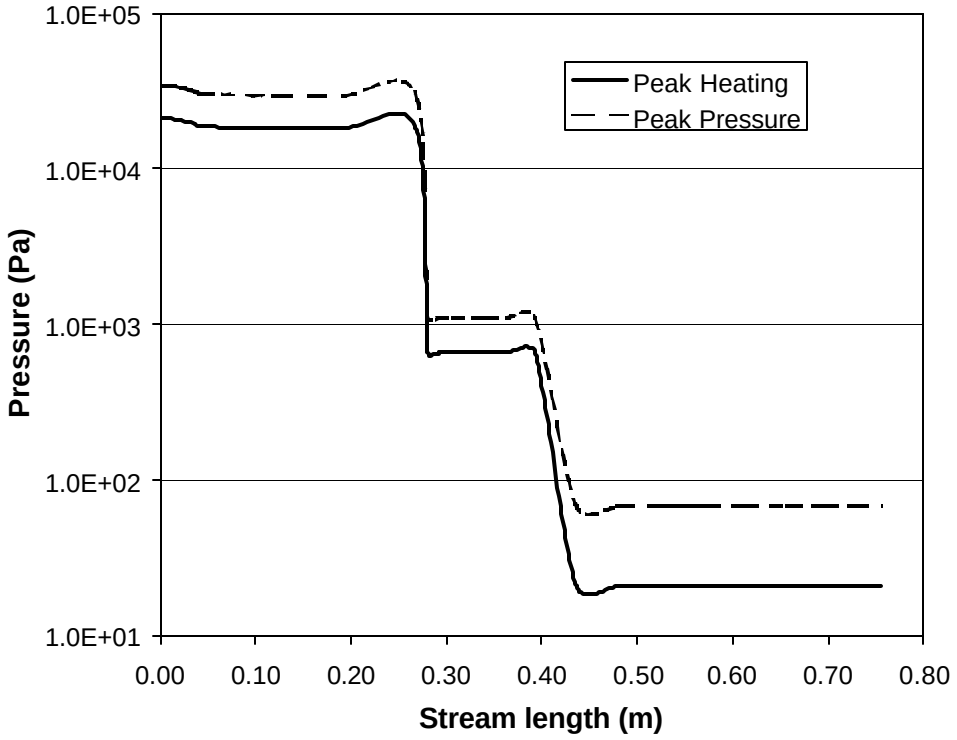

Figure 27: Pressure Distributions over the EDL at Peak Heating and Pressure

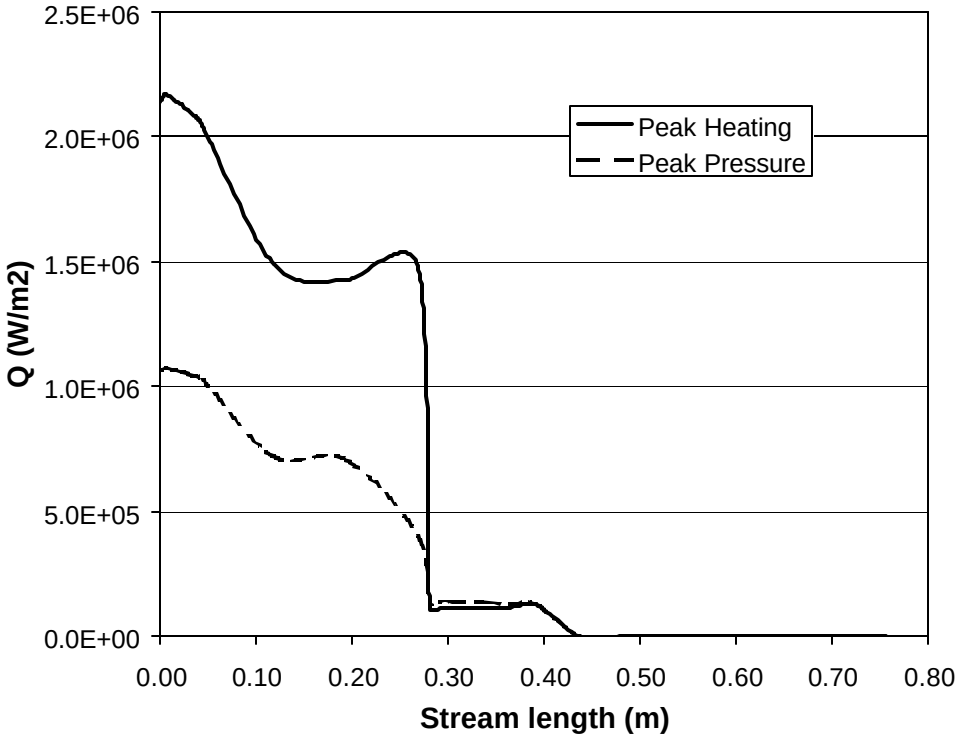

Figure 28: Heating Distributions over the EDL at Peak Heating and Pressure

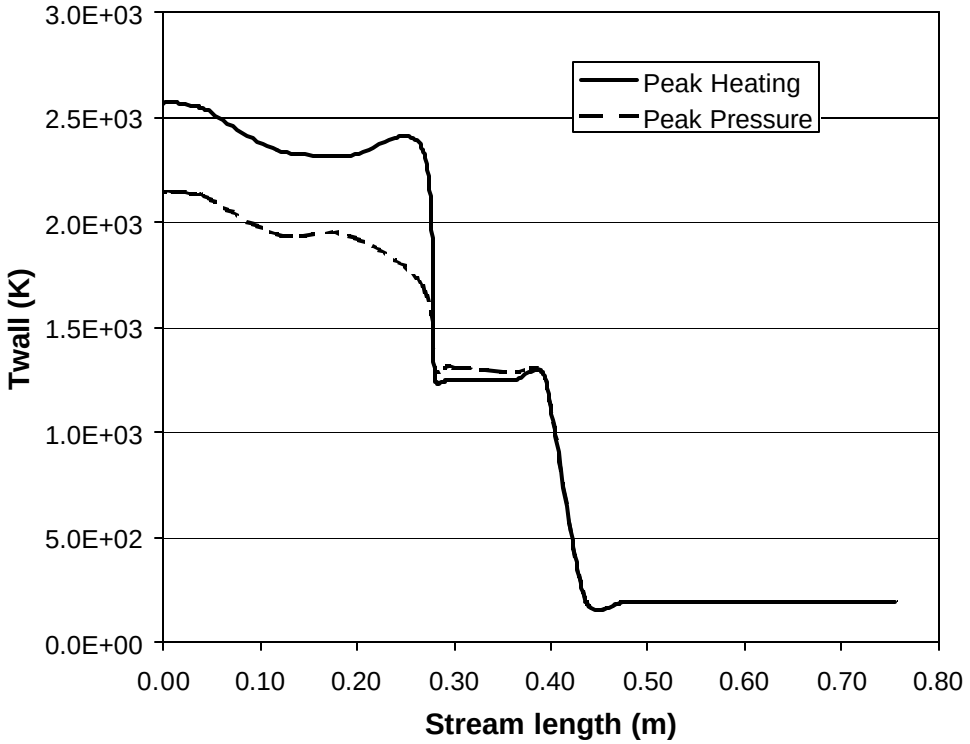

Figure 29: Predicted Wall Temperature Distribution at Peak Heating and Pressure

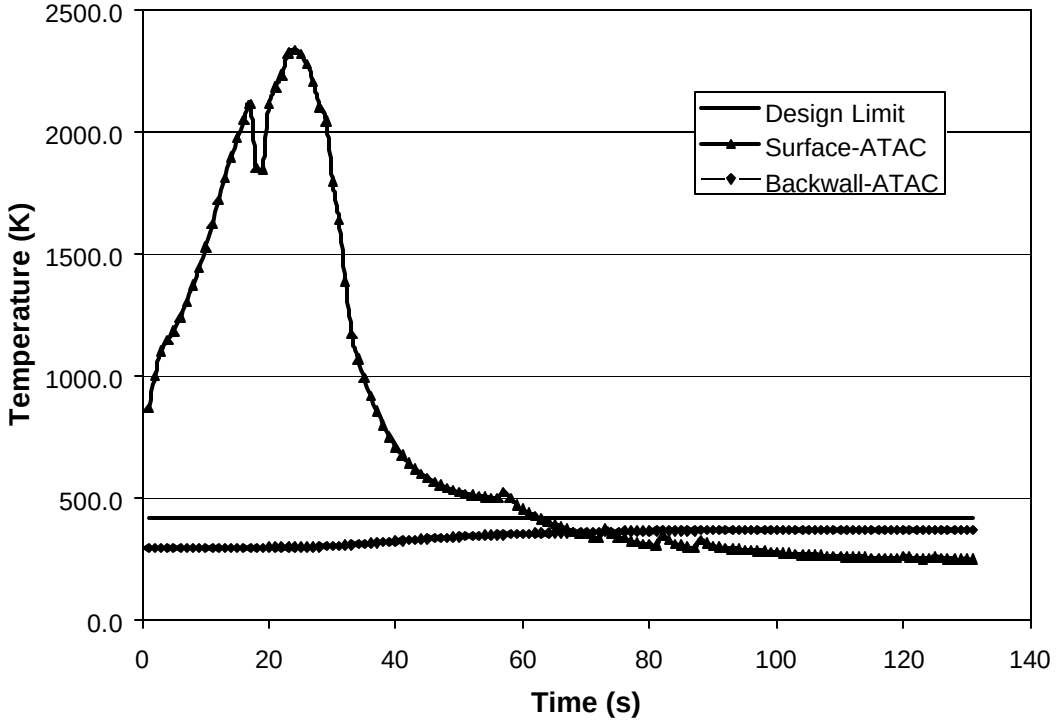

Figure 30: Predicted Stagnations Point Surface and Backwall Temperatures Using 11 mm of Acusil 2

The time history of the surface and backwall temperatures at the stagnation point is shown in Figure 30. The heatshield consists of 11 mm of Acusil 2 on this part of the vehicle. The surface temperature peaks near 2400 K but drops rapidly after 25 seconds. The heatshield continues to absorb the heating as shown by the increase in the temperature at the backwall. Even with this long thermal soak time, the backwall temperature does not exceed the design limit.

Contour plots of the surface heat flux and predicted surface temperatures are shown in Figure 31. These plots also show that the pressure is reasonably constant over the heatshield. The gradient in the heat flux is clearly visible by the change in the contours downstream of the stagnation point.

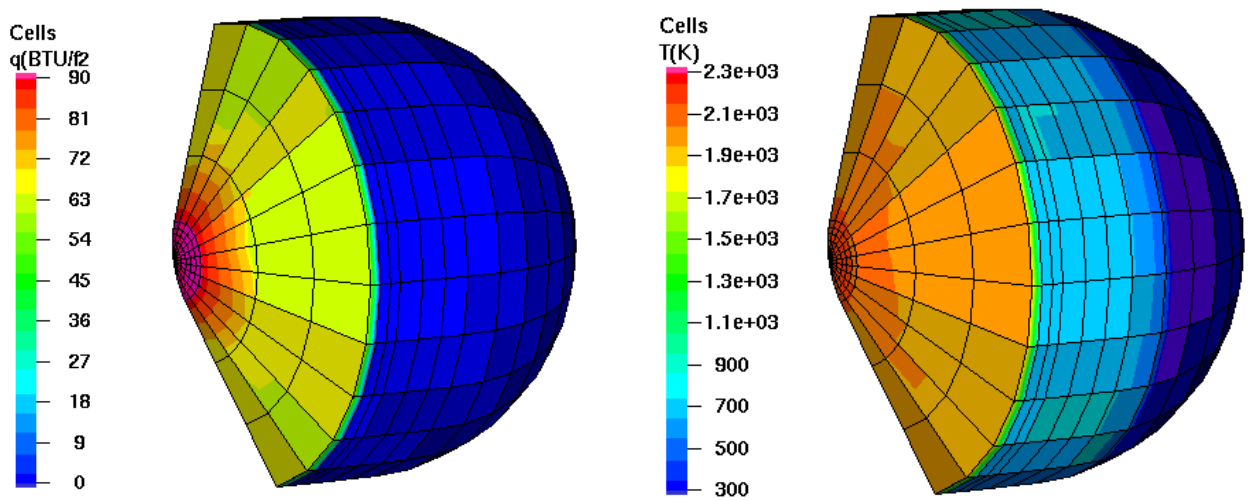

Figure 31: Contour Plots for the Heat Flux and Temperature

To demonstrate the efficiency of ATAC, the Apollo flight calculation used 20 patches to describe the geometry. The actual flight time modeled was 920 sec and 80 CMA solutions were done over the surface of the vehicle. The calculation required 35.84 seconds on a 1.5 GHz Intel processor.

CONCLUSIONS

A new analytical tool has been developed by combining the 1D in-depth thermal analysis technique of CMA with the three-dimensional flowfield and geometry models of MASCC. The new code (ATAC) allows a users to include the effects of ablation, surface temperature, shape change, and pyrolysis gases in a thermal analysis without requiring the extensive amount of labor needed for manually iterating between CMA and MASCC. Comparisons with data from Apollo wind tunnel tests showed that the code was capable of providing good solutions at zero angle of attack and reasonably good solutions at 25 degrees angle of attack. Comparisons with Apollo flight data also showed that good agreement with thermocouple data near the surface. At deeper locations, the predictions were in good agreement in the early parts of the flight but did not model the continued recession of the pyrolysis region. This may be caused by the lack of the coking models in the CMA portion of ATAC. Comparisons with CFD

predictions on the Pascal EDL module showed that the code gave good predictions of the aerodynamic coefficients throughout the entire flight regime. ATAC has been shown to be an efficient and reasonably accurate tool for thermal analysis.

REFERENCES

1. Murray, A. L., "User's Manual for the Maneuvering Aerotherm Shape Change Code (MASCC99)," Aerotherm Corporation, FR 6002-99-001, Huntsville, AL, Jan 1999.
2. "User's Manual: Aerotherm Charring Material Thermal Response and Ablation Program," Acurex Corporation, UM-87-11/ATD, Mt. View, CA, Aug, 1987.
3. Murray, A. L., "User's Manual for the Aeroheating and Thermal Analysis Code (ATAC3D)", ITT Aerotherm, FR 0608A-01-001, Huntsville, AL, Jan 2001.
4. Coons, S. A. and Herzog, B., "Surfaces for Computer-Aided Aircraft Design," AIAA Paper 67-895, 1967.
5. King, H. C., Muramoto, K. K., Murray, A. L., and Pronchick, S. W., "ABRES Shape Change Code (ASCC86): Technical Report and User's Manual," Acurex Corporation, FR-86-24/ATD, Mt View, CA, Dec 1986.
6. Andrews, J. S., "Steady State Airload Distribution on Hammerhead Shaped Payload of a Multistage Vehicle at Transonic Speeds," Boeing Company, D2-22947-1, Seattle, WA, Jan 1964.
7. Isaacson, L. K. and Jones, J. W., "Prediction Techniques for Pressures and Heat-Transfer Distributions Over Bodies of Revolution in High-Subsonic to Low-Supersonic Flight," Naval Weapons Center, NWC TP 4570, China Lake, CA, Nov 1968.
8. Timmer, H. G., "Ablation Aerodynamics for Slender Reentry Bodies," Air Force Flight Dynamics Laboratory, AFFDL-TR-70-27, Dayton, OH, Mar 1970.
9. Kutateladze, S. S. and Leont'ev, A. I., *Turbulent Boundary Layers in Compressible Gases*, Academic Press, 1964.
10. Kutateladze, S.S., "On the Turbulent Boundary Layer with Vanishing Viscosity," *Heat and Mass Transfer in Boundary Layer*, edited by N. Afgan, Z. Zaric, and P Anastasijevic, Volume 1, Proceedings of the International Summer School, Herceg Novi, Beograd, Sep 1968.
11. Bertin, J. J., "Wind-Tunnel Heating Rates for the Apollo Spacecraft," NASA TM X-1033, Jan 1965.
12. Marvin, J., Tendeland, T., and Kussoy, M., "Apollo Forebody Pressure and Heat-Transfer Distributions in Helium at M_∞=20," NASA Ames Research Center, NASA TM X-854, Moffett Field, CA, Nov 1963.
13. Bartlett, E., Abbett, M., Nicolet, W., and Moyer, C., "Improved Heat-Shield Design Procedures for Manned Entry Systems; Part II, Application to Apollo", Aerotherm Corporation, FR 70-15, Part II, Mt. View, CA, Jun 1970.
14. "Postlaunch Report for Mission AS-202 (Apollo Spacecraft 011)," NASA Manned Spacecraft Center, Report MSC-A-R-66-5, Houston, TX, Oct 1966.

NOMENCLATURE, ACRONYMS, ABBREVIATIONS

A	reference area, m^2
B'	non-dimensional mass loss rate, $\dot{m} / r_e u_e C_M$
c_p	specific heat at constant pressure, J/kg-K
$C_f/2$	friction factor, $t_w / r_e u_e^2$
C_h	Stanton number
C_M	mass transfer coefficient
F	entrainment shape factor, $(d - d_e^*)/\Theta$; radiation view factor
h	enthalpy, J/kg
h_r	recovery enthalpy, J/kg
h_s	enthalpy of surface material, J/kg
h_g	enthalpy of pyrolysis gas, J/kg
h_t	total enthalpy $\equiv h + u^2/2$, J/kg
h_w	wall enthalpy, J/kg
H	shape factor, d^*/Θ
$I_{x,y,z}$	influence coefficient
k	thermal conductivity, W/m-K
$\dot{m}$	mass flux, kg/s
$\hat{n}$	surface normal unit vector
p	pressure, N/m^2
Pr	Prandtl number
$\dot{q}_{cond}$	conduction heat flux into material, W/m^2
$\dot{q}_{rad}$	radiation heat flux,, W/m^2
$\dot{q}_w$	wall heat flux, W/m^2
r	radial coordinate, m
Re	Reynolds number
R	recovery factor; gas constant, J/kg-K
s	stream length measured from the stagnation point, m
$\dot{s}$	recession rate in the surface normal direction, m/s
T	temperature, K
u	boundary layer flow velocity tangent to surface, m/s
v	boundary layer flow velocity normal to surface, m/s
$\vec{v}$	tangential velocity vector, m/s
$\vec{V}_\infty$	freestream velocity vector, m/s
$\bar{y}$	shock radial location through which boundary layer edge streamline passes, m
x	coordinate normal to ablating surface with origin fixed in space, m
z	coordinate normal to ablating surface with origin fixed to the receding surface, m

Z_i	diffusion driving potential
d	boundary layer thickness, m
d^*	boundary layer displacement thickness $\equiv \int_0^d 1-\left(\frac{r\,u}{r_e u_e}\right)dy$, m
e	surface emissivity
q	time, s
Θ	boundary layer momentum thickness, m
m	viscosity, kg/m-s
r	density, kg/m^3
Φ	energy thickness $\equiv \int_0^d \frac{r\,u}{r_e u_e}\left(\frac{h_{t,i}-h_t}{h_{t,e}-h_w}\right)dy$, m

Subscripts

c	char property
e	boundary layer edge
g	pyrolysis gas property
ℓ	laminar flow
t	turbulent flow
w	wall